



Thermally Drawn Flexible Fiber Sensors: Principles, Materials, Structures, and Applications

Cite as

Nano-Micro Lett.
(2026) 18:4

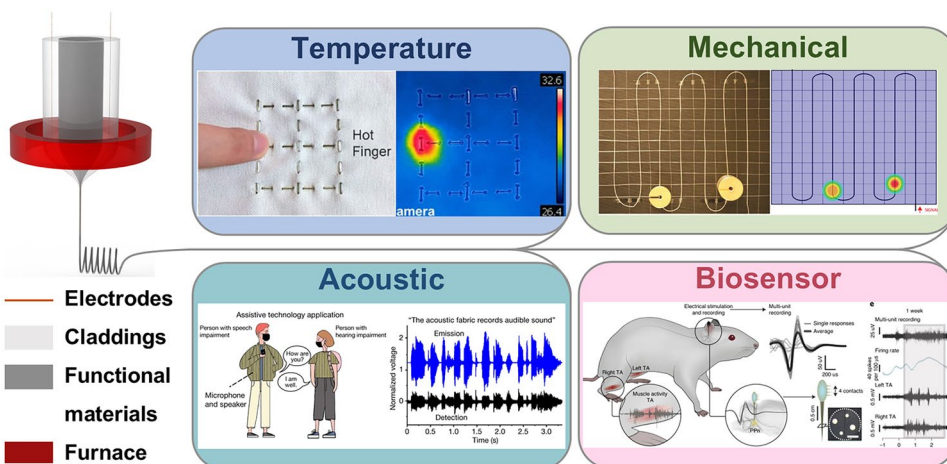
Received: 16 March 2025
Accepted: 15 June 2025
© The Author(s) 2025

ZhaoLun Zhang^{1,2,3}, Yuchang Xue^{1,3}, Pengyu Zhang^{1,3}, Xiao Yang^{1,2,3,4}, Xishun Wang⁵ ✉, Chunyang Wang^{1,3,4}, Haisheng Chen^{1,2,3,4} ✉, Xinghua Zheng^{1,3,4} ✉, Xin Yin⁶ ✉, Ting Zhang^{1,2,3,4,7,8} ✉

HIGHLIGHTS

- The review briefly introduces the principle, material selection criteria, and development of the thermal drawing process.
- Based on different stimuli, the review comprehensively summarizes the latest progress in thermally drawn temperature, acoustic, mechanical, chemical, biological, optoelectronic, and multifunctional sensors.
- The review discusses the future development trends of thermally drawn fiber sensors in terms of material, structure, fabrication, function, and stability.

ABSTRACT Flexible fiber sensors, However, traditional methods face challenges in fabricating low-cost, large-scale fiber sensors. In recent years, the thermal drawing process has rapidly advanced, offering a novel approach to flexible fiber sensors. Through the preform-to-fiber manufacturing technique, a variety of fiber sensors with complex functionalities spanning from the nanoscale to kilometer scale can be automated in a short time.



Examples include temperature, acoustic, mechanical, chemical, biological, optoelectronic, and multifunctional sensors, which operate on diverse sensing principles such as resistance, capacitance, piezoelectricity, triboelectricity, photoelectricity, and thermoelectricity. This review outlines the principles of the thermal drawing process and provides a detailed overview of the latest advancements in various thermally drawn fiber sensors. Finally, the future developments of thermally drawn fiber sensors are discussed.

KEYWORDS Thermally drawn fiber sensors; Sensing principles; Temperature sensors; Mechanical sensors; Multifunctional sensors

✉ Xishun Wang, wangxishun96@163.com; Haisheng Chen, chen_hs@iet.cn; Xinghua Zheng, zhengxh@iet.cn; Xin Yin, yinxin304@126.com; Ting Zhang, zhangting@iet.cn

¹ Institute of Engineering Thermophysics, Chinese Academy of Sciences, Beijing 100190, People's Republic of China

² Nanjing Institute of Future Energy System, Nanjing 211135, People's Republic of China

³ University of Chinese Academy of Sciences, Beijing 100049, People's Republic of China

⁴ Key Laboratory of Long-Duration and Large-Scale Energy Storage, Chinese Academy of Sciences, Beijing 100190, People's Republic of China

⁵ Department of Orthopedics, Capital Center For Children's Health, Capital Medical University, Beijing 100020, People's Republic of China

⁶ Department of Orthopedics, Fourth Medical Center of PLA General Hospital, Beijing 100048, People's Republic of China

⁷ University of Chinese Academy of Sciences, Nanjing 211135, People's Republic of China

⁸ Innovation Academy for Light-Duty Gas Turbine, Chinese Academy of Sciences, Beijing 100190, People's Republic of China

Published online: 18 July 2025



SHANGHAI JIAO TONG UNIVERSITY PRESS

Springer

1 Introduction

In recent decades, flexible electronics have advanced rapidly. Due to their bendable and stretchable properties, flexible electronic products have been widely applied in biomedicine, intelligent robotics, environment, and health monitoring [1–10], profoundly transforming people's lives. As a key component of flexible electronics, sensors act as a bridge connecting humans with the external environment. They can convert external stimuli into real-time electrical signals (such as capacitance and resistance) with high reliability and sensitivity. Their application demands are increasing significantly [11–14]. In the early research on flexible sensors, most sensing elements were fabricated by combining inorganic rigid materials (such as Si and Au) with flexible substrates [15–17]. However, these partially flexible sensors were difficult to apply to complex surfaces such as human skin and robots. As a result, fully flexible sensors based on flexible and stretchable materials like organic materials and metal nanowires have emerged rapidly [18, 19]. Depending on the fabrication method, flexible sensors can be classified into film and fiber-based sensors [20, 21]. Compared to film, fiber, as the smallest unit in the textile industry, offers better breathability and wearing comfort while maintaining excellent flexibility and biocompatibility, making it more advantageous for applications in smart textiles and wearable devices [22–24].

From natural fibers to synthetic fibers and further to revolutionary carbon fibers and optical fibers, multi-functionalization has always been the development trend of fibers [25–28]. To date, various methods such as dry spinning [29], wet spinning [30], melt spinning [31], microfluidic spinning [32], electrospinning [33, 34], physical vapor deposition (PVD) [35], chemical vapor deposition (CVD) [36], and 3D printing [37] have been applied to fabricate multifunctional fiber sensors. However, they all have some insurmountable disadvantages. Spinning processes often involve multiple processing steps and prolonged overall fabrication times [38]. Moreover, microfluidic spinning process is more complex in terms of its process [32]. PVD and CVD typically require harsh conditions such as high-temperature and high-vacuum environment [39]. 3D printing of fibers is constrained by limited printable lengths and inherently slow deposition rates [38]. Among these processes, thermal drawing process stands out as a superior technology: it obviates the need for complex environment, enables customization of

diverse fiber architectures, and supports functional integration across length scales spanning from nanometers to kilometers [39]. This technique represents the most promising pathway for low-cost, large-scale production of functional fibers, with exceptional industrial applicability. Furthermore, this process has excellent process compatibility. Its combination with various technologies such as 3D printing, direct imprinting, and photolithography can further promote the high-performance and multifunctional applications of thermally drawn fiber sensors (TDFSs) [40–42].

The third revolution of science and technology is driving the rapid development of the Internet of Things (IoT) and flexible electronics. It is urgent to increase the integration of flexible sensors and simplify wearable device structures [12]. Recently, Moore's law for thermally drawn fibers has been proposed, indicating the continuous high integration of materials and devices in TDFSs [43], giving a powerful boost to the advancement of flexible sensors. Although a few years ago, previous reviews have summarized the thermal drawing process and its diverse applications [44–47]. TDFSs have undergone substantial expansion in both research domains and novel applications in recent years. There is a pressing need to systematically summarize their latest advancements, analyze future development tendency, and provide a consolidated reference for researchers working in this rapidly evolving field. Therefore, this article will introduce the mechanism and development trend of the thermal drawing process, review common sensing principles, and provide a detailed discussion of the applications of TDFSs in temperature, mechanical, acoustic, chemical, biological, optoelectronic, flow, and humidity sensing (Fig. 1). Finally, the future development directions of TDFSs are discussed. This review aims to guide the development of flexible fiber sensors.

2 Thermal Drawing Process

The thermal drawing process is an emerging fiber fabrication method initially used to fabricate optical fibers [54, 55]. Due to its capability to control fiber structures and sizes, it has garnered significant attention in materials science and textiles. Compared to traditional fiber fabrication methods, the thermal drawing process enables the rapid, large-scale, and automated production of multimaterial fibers incorporating high-density devices and diverse functionalities.

This technology aligns well with the requirements of textile manufacturing processes, providing a universal platform for the scalable production of smart textiles.

2.1 Mechanism of the Thermal Drawing Process

The mechanism of the thermal drawing process is to integrate fiber formation and functionalization into a continuous drawing process. During this process, all components (including claddings, electrodes, functional materials, etc.) are co-drawn in a viscous molten state [56]. The first step in the specific process is to fabricate a macroscopic preform. The preform, which serves as an enlarged model of the fiber, is the crucial component of the thermal drawing process. Various methods can be used to fabricate preforms, such as rod-in-tube [57], hot pressing [58], stack-and-draw [59], thermal consolidation [60], film rolling [61], 3D printing [62], double-crucible [63], and melt casting [64]. The preform is then mounted in a drawing tower, passing sequentially through the preheating zone, heating zone, and insulation zone from top to bottom. It is gradually heated to 50–100 °C above the cladding’s glass transition temperature (T_g) or melting temperature (T_m). After maintaining this temperature for a period, the preform undergoes necking. At

this stage, the fiber is drawn under external force, enabling continuous and controllable production (Fig. 1). The resulting fiber retains the same composition and structure as the preform but with a diameter reduced to the submillimeter scale, integrating multiple materials and functionalities.

The diameter of the fiber can be adjusted by thermal drawing parameters, including the drawing temperature (T_D), the fiber drawing speed (v_d), and the preform feeding speed (v_f). According to the law of volume conservation, the fiber diameter (D_{fiber}) can be expressed as:

$$D_{\text{fiber}} = D_{\text{preform}} \times \sqrt{\frac{v_f}{v_d}} \tag{1}$$

The above formula is merely a simple reference for controlling fiber diameter. It is important to note that thermal drawing is a complex process, and various factors such as material viscosity, thermal expansion coefficient, chemical stability, and surface tension [65] can also influence it. These factors are not accounted for in the formula. Additionally, to increase the drawing stress for stabilizing the fiber dimensions, it is often necessary to reduce the temperature [66].

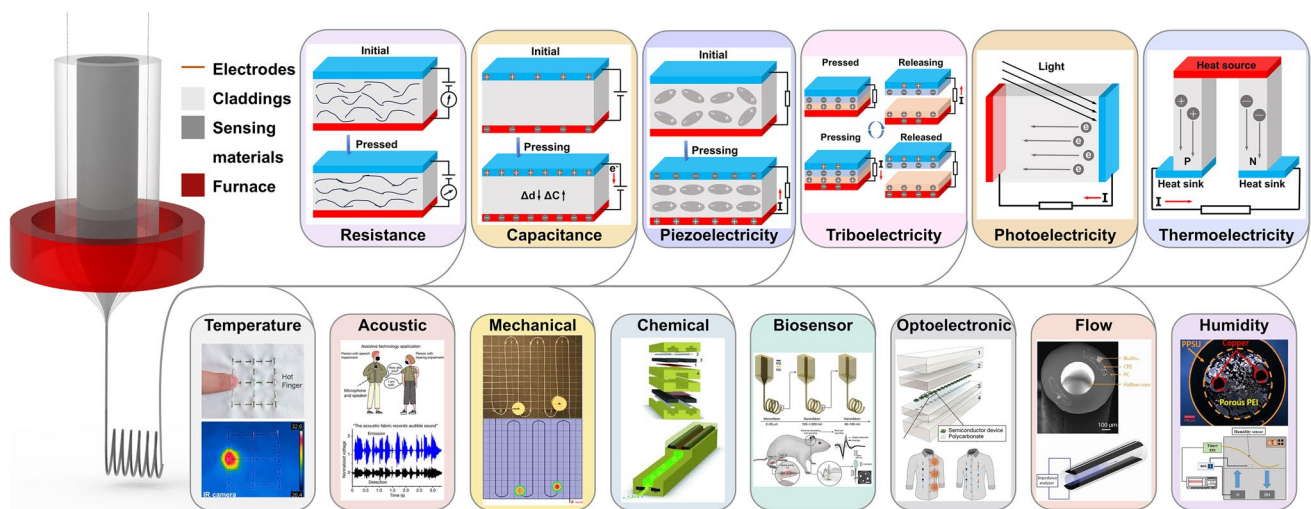


Fig. 1 Sensing principles and applications of thermally drawn fiber sensors. Sensing principles: resistance, capacitance, piezoelectricity, triboelectricity, photoelectricity, and thermoelectricity. Applications: Temperature sensor. Reproduced with permission [48] Copyright 2019 American Chemical Society. Mechanical sensor. Reproduced with permission [49] Copyright 2020 Wiley. Acoustic sensor. Reproduced with permission [19] Copyright 2022 Springer. Chemical sensor. Reproduced with permission [50] Copyright 2012 Wiley. Biosensor. Reproduced with permission [51] Copyright 2022 Springer. Optoelectronic sensor. Reproduced with permission [43] Copyright 2018 Springer. Flow sensor. Reproduced with permission [52] Copyright 2019 Wiley. Humidity sensor. Reproduced with permission [53] Copyright 2019 Multidisciplinary Digital Publishing Institute

Table 1 T_g , VST, and α of common polymers

Materials	T_g (°C)	VST (°C)	α (10^{-6} m/(m °C))
PC	139–150	123–157	65–70
PMMA	100–120	87–125	50–90
SEBS	– 90	~ 165	61–65
LDPE	– 110	90–125	108–200
PVDF	– 42 to – 25	~ 136	128–140
PSU	187–190	175–185	55–60
PEI	217–220	210–226	~ 100
TPU	– 49 to – 12	66–145	~ 57
PS	63–112	~ 120	~ 70

2.2 Material Selection Criteria

Although the thermal drawing process theoretically enables the co-drawing of multiple materials, differences in the thermal, mechanical, and chemical properties of various materials can affect the uniformity of fiber structure and cross-sectional integrity along the fiber length. Therefore, certain criteria must be followed when selecting materials.

Firstly, all co-drawn materials should have similar T_g or T_m , and the drawing temperature must be higher than the T_g or T_m but lower than the boiling temperature [67]. Secondly, to prevent fractures and cracks, materials should also exhibit similar thermal properties, such as Vicat softening temperature (VST) [68], thermal expansion coefficients (α), and viscosities. This helps control residual stresses caused by thermal–mechanical mismatch in fiber [69]. Table 1 summarizes the T_g , VST, and α of common polymers. Additionally, materials should demonstrate good adhesion and wettability in both viscous and solid states to avoid cracking after rapid thermal cooling and quenching [70]. Furthermore, since the cladding bears most of the stress, the process must occur within a relatively high-viscosity range, typically between 10^4 and 10^8 Pa s [56]. It is noteworthy that viscosity exhibits significant temperature dependence, and determining whether the viscosity of specific materials matches requirements typically necessitates analysis with rheometer. Ideal cladding should be amorphous. In addition to conventional glass materials, thermoplastic materials can also serve as claddings for TDFSs. For instance, highly transparent materials such as polymethyl methacrylate (PMMA) and polycarbonate (PC) find extensive applications in the field of bio-sensing [71]. Meanwhile, thermoplastic elastomers (TPEs) that meet rheological criteria like SEBS play an indispensable role in acoustic and mechanical sensing due to their

unique properties [19, 72, 73]. Notably, the thermal drawing process induces molecular chain realignment in polymers. Taking P(VDF-TrFE) as an example, spontaneous α -phase to β -phase transition occurs during this process, leading to altered material properties. This transformation mechanism also necessitates consideration in material selection. Finally, potential chemical diffusion and reactions must also be considered [56].

2.3 Development Trend of the Thermal Drawing Process

Over decades of development in the thermal drawing process, three types of thermally drawn fibers have emerged based on differences in structure and fabrication processes. In 2002, the first generation of thermally drawn fiber was fabricated by Yoel Fink's group at the Massachusetts Institute of Technology (MIT), representing the initial structure and fabrication process [54, 55]. These fibers were directly drawn from preforms without post-processing, maintaining continuous and uniform composition across their entire length. During the thermal drawing process, only physical contraction of the preform occurred, and it was impossible to adjust or customize the structure along the fiber length. In 2012, the second generation of thermally drawn fiber was fabricated, incorporating post-processing steps into the first generation [74]. For example, during a post-processing step involving thermal perturbation that causes capillary rupture, the cylindrical fibers evolve toward more stable spherical shapes due to the Rayleigh instability phenomenon when subjected to thermal disturbances [75]. In 2018, the third generation of thermally drawn fibers emerged. These fibers featured pre-designed empty slots for electrodes or micro-devices within the preform, enabling the gradual establishment of electrical contacts during the drawing process [43]. Based on this advancement, fibers containing a series of microdevices were fabricated [43, 76, 77]. Concurrently, Yoel Fink's group proposed the concept of "Moore's law for fibers" [43]. Analogous to Moore's law in microelectronics, this principle predicts the continuous high-density integration of functional materials and devices into fibers and textiles, paving the way for smart textiles with broader applications and even computationally predictable functionalities. In the future, thermally drawn fibers will evolve toward more diverse material selections, complex structures, and highly

integrated functionalities. They will also become more closely integrated with artificial intelligence and machine learning. Smart textiles based on thermally drawn fibers will further transcend the limitations of conventional products, evolving into sophisticated computational platforms to serve human life.

3 Applications of Thermally Drawn Fiber Sensors

In recent years, thermally drawn fiber sensors (TDFSs) have developed rapidly. Various sensors have been fabricated based on principles such as resistance, capacitance, piezoelectricity, triboelectricity, photoelectricity, and thermoelectricity. These sensors cover multiple functions, including temperature, acoustic, mechanical, chemical, biological, optoelectronic, flow, and humidity sensing. Table 2 summarizes the principles, functional materials, claddings, and electrodes of the eight main types of sensors. This chapter introduced the latest advancements in each field according to different sensor types.

3.1 Temperature Sensors

Temperature sensors are among the most widely used sensors in military, medical, biological, and industrial fields. Monitoring temperature can reveal a wealth of chemical, physical, and biological information, which is helpful for practical applications. The principles of temperature sensors mainly include thermistor, thermoelectric effect, capacitance, and infrared imaging [48, 88, 89]. Among these, infrared imaging has difficulty monitoring irregular surfaces' temperature. Besides, it is limited by space and relatively expensive [90]. Therefore, it is generally not used in flexible temperature sensors. Temperature sensors based on thermistors convert temperature changes into resistance changes. Their principle is based on the following formula:

$$R = \rho \frac{L}{A} \quad (2)$$

In the formula, ρ , L , and A denote the resistivity, length, and cross-sectional area of the sensing material, respectively. Generally, the resistance change mainly consists of two parts: the geometry change and the resistivity change [91]. In some semiconductors, the effect of temperature on resistivity constitutes the main part of the resistance change. The temperature coefficient of resistance (TCR), which represents the ratio of resistance change to temperature change,

Table 2 Summary of the principles, functional materials, claddings, and electrodes for eight types of sensors

Sensor types	Principles	Functional materials	Claddings	Electrodes	References
Temperature sensors	Resistance	rGO/PLA	PS	rGO/PLA	[78]
	Thermoelectricity	SEBS	SEBS	Dual GaInSn	[79]
	Capacitance	LDPE	LDPE	Copper wire	[49]
Acoustic sensors	Piezoelectricity	P(VDF-TrFE)/BaTiO ₃	SEBS	CPE and copper wire	[19]
Mechanical sensors	Resistance	CPE	SEBS	CPE	[80]
	Capacitance	Galinstan	SEBS	Galinstan	[72]
	Piezoelectricity	BTO-PVDF	PC	C-LDPE	[81]
	TENG	PVDF	PVDF	CPE	[41]
	Photoelectricity	STPU	STPU	–	[82]
Chemical sensors	Photoelectricity	Se ₉₇ S ₃	PSU	Sn ₆₃ Pb ₃₇	[50]
	Electrochemistry	CPC and Pt-MG	PEI	CPC and Pt-MG	[83]
Biosensors	Photoelectricity	PC/PMMA	PDMS	CNT sheets	[84]
	Capacitance	COC	PC	CPE with 2% CNF	[85]
	TENG	PVDF	PSU	Copper tape	[86]
Optoelectronic sensors	Photoelectricity	Ge	PC	Copper wire	[87]
Flow sensors	Capacitance	Fluid in the microfluidic channel	PC	CPE and Bi ₅₈ Sn ₄₂	[52]
Humidity sensors	Capacitance	Porous PEI	PPSU	Copper wire	[53]



is an indicator of thermistor performance [92]. Chalcogenide semiconductors are commonly used in temperature sensors [93]. Mehmet et al. [93] firstly fabricated a temperature sensor using the chalcogenide semiconductor $\text{Ge}_{17}\text{As}_{23}\text{Se}_{14}\text{Te}_{46}$ (GAST) as the thermistor via the thermal drawing process. They selected 96%Sn–4%Ag alloy electrodes and polysulfone (PSU) polymer cladding. The final fiber is shown in Fig. 2a. The electrical signal of a single fiber was proportional to the integral of thermal excitation over its entire length. Fiber maintained good ohmic characteristics at both low (11 °C) and high temperatures (58 °C). To measure the spatial temperature, an 8×8 fiber array with 1 cm spacing was further fabricated (Fig. 2b) and woven into a fabric, capable of precisely locating heat sources and quantifying temperature (Fig. 2c, d). The high modulus of semiconductors and metal electrodes limits the application of fibers in wearable devices, while the TCR of polymers is not as significant as that of semiconductors. Graphene, with its excellent electrical properties and unique temperature response characteristics, has been widely used in temperature sensors [94, 95]. Adding it into polymers can enhance the TCR while maintaining flexibility. Ryu et al. [78] fabricated a TDFS using reduced graphene oxide (rGO) and polylactic acid (PLA) as the thermistor. The outer layers consisted of linear low-density polyethylene (LLDPE) and a sacrificial polystyrene (PS) cladding, as shown in Fig. 2e, f. When woven into a glove, it could detect touch temperature (Fig. 2g, h). Moreover, the fiber exhibited consistent and reliable temperature responses under repeated mechanical stress and chemical exposure, meeting the requirements for long-term applications in flexible wearable fiber sensors.

Different from traditional thermistor-based temperature sensors, Loke et al. [77] integrated hundreds of dispersed thermistors and storage elements into the interior of a thermally drawn fiber, as shown in Fig. 2i, j. A single node at the end of the fiber can independently access multiple devices inside the fiber. A single fiber achieves the functions of temperature monitoring and storage simultaneously, overcoming the previous limitation of relying on parallel connections of multiple devices. When woven into a shirt (Fig. 2k), the fiber could monitor body temperature under various human motions and continuously store temperature data for several days. Furthermore, through a neural network, by analyzing the unknown temperature–time data, the type of physical activity could be inferred with an accuracy of 96%. This fiber can perform different functions at different

positions, reducing the number of devices required for the same function and improving the integration level of flexible electronics.

The thermoelectric (TE) effect refers to the energy conversion between heat and electricity, including the Seebeck effect, Peltier effect, and Thomson effect. Temperature sensors based on the thermoelectric effect mainly utilize the Seebeck effect, which means that a temperature gradient creates a potential difference between the contact surfaces of different materials. In a closed circuit, this potential difference will generate an electric current, thereby converting thermal energy into electrical energy [96]. The potential difference V can be expressed by the following formula:

$$V = S\Delta T \quad (3)$$

In the formula, S is the relative Seebeck coefficient, and ΔT is the temperature difference. Therefore, materials with high Seebeck coefficients are crucial for high-sensitivity and high-resolution temperature measurements [97]. The thermoelectric performance of amorphous semiconductor glass $(\text{Te}_{85}\text{Se}_{15})_{45}\text{As}_{30}\text{Cu}_{25}$ is moderate, but its Seebeck coefficient is relatively high. Zhang et al. [48] used it as the functional material and polyethyleneimine (PEI) as the cladding to fabricate the temperature sensor shown in Fig. 2l. The fiber can operate in a wide temperature range of up to 150 °C. A single fiber can quantify the temperature at a fixed position with a temperature resolution as high as 0.05 °C, and it can also locate the heat source at the millimeter level under a fixed temperature. Further, to achieve simultaneous temperature monitoring and localization, a 3×3 fiber array was constructed, as shown in Fig. 2m. A spatial temperature resolution of N^2 can be achieved with only $2N$ fibers. This fiber array has ultra-high flexibility and can monitor temperature over a large area with high resolution.

In addition to thermistors and the thermoelectric effect, combining capacitors with the interdisciplinary measurement technique of frequency-domain reflectometry [49] can also be used for distributed temperature sensing. A capacitive sensor consists of the upper and lower electrode and a dielectric layer in between. In practical applications, most capacitive sensors can be regarded as parallel-plate capacitors, and the capacitance calculation formula is as follows:

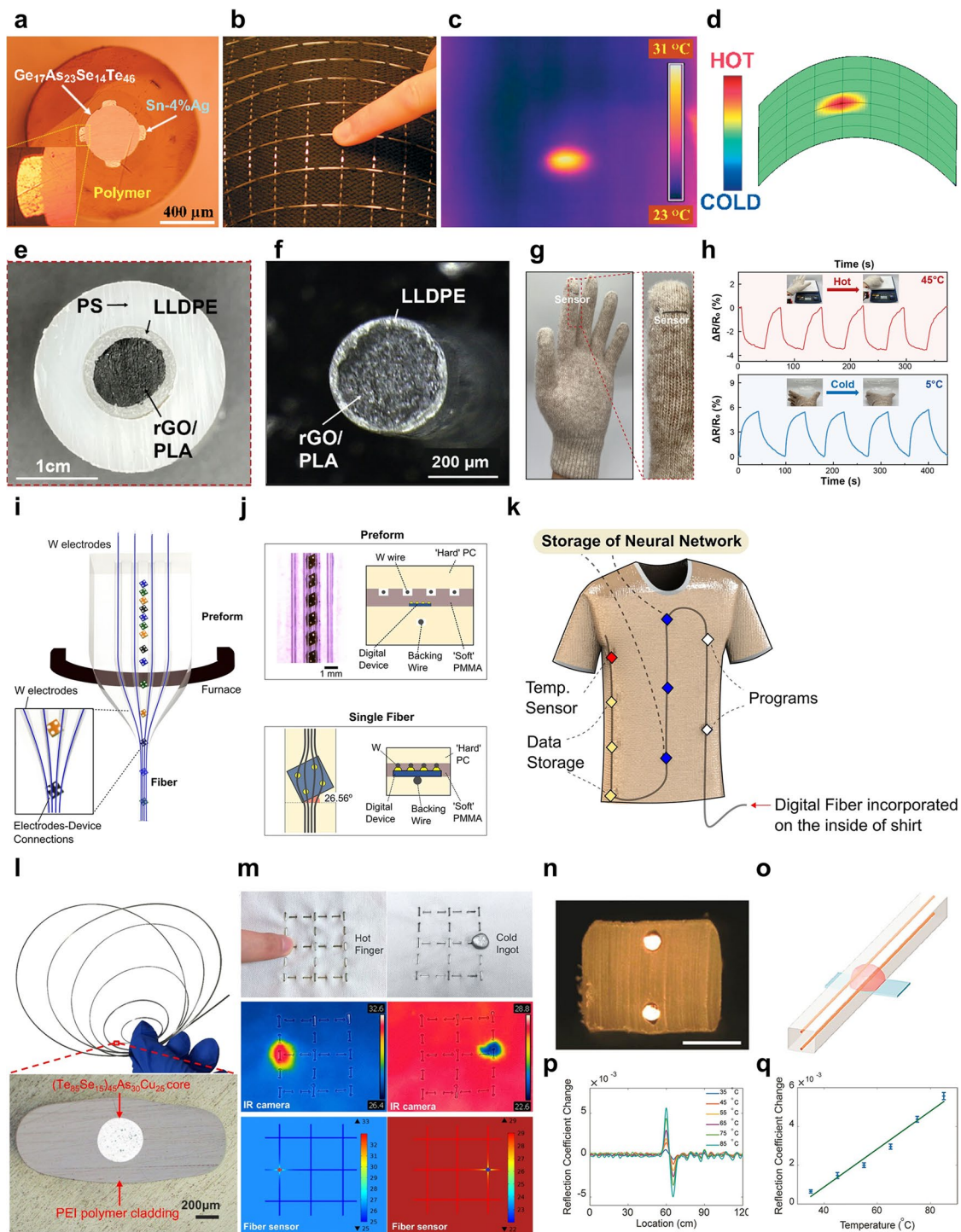


Fig. 2 Thermally drawn fibers for temperature sensing. **a** A Micrograph of the cross section of a thermistor-based fiber sensor. **b** Fiber array for spatial sensing. **c, d** Infrared radiographs and thermal maps of fiber array. Reproduced with permission [93] Copyright 2006 Wiley. **e, f** Structure of the perform and fiber with rGO/PLA thermistor in the core. **g, h** Image of the TDFS sewn into the top of a glove and temperature test with multiple touches. Reproduced with permission [78] Copyright 2023 Springer. **i, j** TDFS with integrated multiple microelectronic components. **k** Shirt integrated with fibers. Reproduced with permission [77] Copyright 2021 Springer. **l** Fiber structure with TE material in the core. **m** Temperature sensor network based on 3 × 3 TE fiber arrays for simultaneous detection and localization of heat source. Reproduced with permission [48] Copyright 2019 American Chemical Society. **n** Fiber structure of the FDR-based TDFS. **o** Image of the fiber being heated at one location. **p, q** Temperature response and reflection coefficient change of the fiber. Reproduced with permission [49] Copyright 2020 Wiley

Table 3 Performance parameters of temperature sensors based on three different principles

Principles	Range (°C)	Sensitivity	Resolution (°C)	Response time (s)	References
Thermistor	25–45	$-0.285\% \text{ } ^\circ\text{C}^{-1}$	1	11.6	[78]
Thermoelectric effect	25–150	–	0.05	3	[48]
Capacitor	25–85	$9.8 \times 10^{-5} \text{ } ^\circ\text{C}^{-1}$	2	–	[49]

$$C = \frac{\epsilon_0 \epsilon_r A}{d} \quad (4)$$

In the formula, C is the capacitance, ϵ_0 is the vacuum permittivity, ϵ_r is the relative permittivity of the dielectric layer, and A and d are the facing area and the distance between the upper and lower electrode, respectively. When subjected to external stimuli, ϵ_r , A , and d may change, causing a change in capacitance [98]. Capacitive sensors have the advantages of high linearity, low hysteresis, and short response time [99]. However, the capacitance change in microcapacitive sensors is small and easily affected by environmental interference, so accompanying signal processing and amplification circuit devices are required [100].

Time-domain reflectometry (TDR) and frequency-domain reflectometry (FDR) were initially developed to detect fault locations in continuous transmission lines. Both techniques rely on vector network analyzers (VNA). TDR sends a high-frequency pulse along the transmission line. The signal is partially reflected at each point where the impedance changes. The location of the interference can be calculated based on the time when the reflected wave reaches the starting point of the line [101]. Different from TDR, FDR sends a set of wideband sinusoidal swept frequency signals into the line. By comprehensively analyzing and processing parameters such as the standing wave, wideband impedance spectrum, and reflection coefficient spectrum of the reflected wave, the location of the interference can be determined [102]. Capacitance is an important component of impedance changes, and combining capacitors with FDR is an effective way to convert external signals into electrical signal outputs.

The thickness and permittivity of some polymers change with temperature. Yu et al. [49] selected low-density polyethylene (LDPE) with a high thermal expansion coefficient as the sensing material and copper wire as the electrodes to fabricate the fiber shown in Fig. 2n. A thermoelectric cooler (TEC) is used to locally heat the fiber (Fig. 2o). The temperature changes cause alterations in the thickness and permittivity of LDPE, increasing the impedance. Based on

the principle of FDR, the reflection signal changes accordingly (Fig. 2p, q), thereby enabling temperature sensing. This method holds great potential for low-cost, distributed temperature sensing.

Table 3 summarizes the performance parameters of temperature sensors based on three different principles. Thermistor-based temperature sensors, with their simple working principle, are the most widely used but exhibit inferior performance. Thermoelectric effect-based sensors achieve the highest resolution and temperature range, surpassing most temperature sensors prepared by other methods [27, 103]. However, their structural complexity limits practical applications. Capacitance temperature sensors enable distributed temperature sensing and simplify system structure, yet their performance requires significant improvement. Future research should focus on enhancing the overall performance of temperature sensors while simplifying their structure and broadening applications.

3.2 Acoustic Sensors

Sound is ubiquitous in nature and human activities. Acoustic sensors play a crucial role in various fields such as natural disaster prediction, ultrasonic imaging of human tissues, and detection of natural gas pipeline leaks [104–106]. The earliest acoustic sensors were rigid [107], which limited their applications. With the development of flexible electronics, the new generation of flexible and wearable acoustic sensors has stood out due to their good flexibility and biocompatibility. The thermal drawing process provides an idea for the large-scale fabrication of acoustic fiber sensors, enhances the applicability of textiles, and can achieve functions such as sound localization and acoustic communication [19, 108].

Most acoustic sensors operate based on the piezoelectric effect. It is a physical phenomenon consisting of two parts: the direct piezoelectric effect and the inverse piezoelectric effect. The direct piezoelectric effect refers to the state

where, without external forces, the positive and negative charges within the piezoelectric material are balanced, and the material is electrically neutral. When subjected to external forces, the material deforms, causing the centers of positive and negative charges to shift, resulting in polarization and the generation of positive and negative charges on two opposite surfaces. When the external force is removed, the piezoelectric material returns to its initial state and becomes non-electrified again. The converse piezoelectric effect, on the other hand, means that when a piezoelectric material is placed in an electric field, it undergoes deformation. When the applied electric field is removed, the piezoelectric material returns to its initial state [109].

The principles of the direct and inverse piezoelectric effects are shown by Hooke's law and electrical equations, respectively:

$$S_T = d_i E \quad (5)$$

$$D_E = d T \quad (6)$$

Further linear approximation leads to the first-type piezoelectric equations [110]:

$$S_i = s_{ij}^E T_j + d_{im} E_m \quad (7)$$

$$D_k = d_{jk} T_j + \epsilon_{km}^T E_m \quad (8)$$

In the formula, D is the electric displacement, d is the piezoelectric constant, T is the stress, S is the strain, E is the electric field strength, s^E is the elastic compliance constant under constant electric field strength, ϵ^T is the permittivity, and i, j, k are the coordinate directions. Among these, the piezoelectric constant d is the most important parameter for measuring the piezoelectric performance of piezoelectric materials. Sensors based on the piezoelectric effect can be self-powered and feature fast response and high sensitivity [111, 112]. However, due to the unique properties of piezoelectric materials, piezoelectric sensors can only detect dynamic pressure changes and are powerless against static pressure. Currently, piezoelectric polymers represented by polyvinylidene difluoride (PVDF) and poly(vinylidene fluoride-trifluoroethylene) (P(VDF-TrFE)) have been widely used in acoustic sensors. However, their piezoelectric constant is much lower than traditional piezoelectric materials

such as piezoelectric ceramics. Therefore, to fabricate higher-sensitivity acoustic sensors, researchers have made many attempts to enhance the piezoelectric performance of fibers by increasing the active area and improving material selection.

In 2010, Egusa et al. [113] first fabricated acoustic fiber sensors via thermal drawing process. In this study, the fibers had two structures: rectangular and concentric. Both fibers used the ferroelectric polymer P(VDF-TrFE) as the piezoelectric layer, indium and carbon-loaded poly(carbonate) (CPC) together as electrodes, and PC as the insulating cladding, as shown in Fig. 3a, b. The fibers exhibited piezoelectric response and acoustic transduction over a frequency range from kilohertz to megahertz. Moreover, the PC cladding enabled the fibers to work underwater. As shown in Fig. 3c, the fibers could function as both sensors and actuators, with piezoelectric responses matching the inherent frequency characteristics of the transducers. Furthermore, a Fabry–Pérot interferometer (FPI) structure, which is an optical cavity composed of two parallel mirrors, was constructed in the fibers. Light is reflected and transmitted multiple times inside the interferometer, generating a series of interference fringes. Only specific wavelengths of light are enhanced through interference, while others are suppressed. Thus, the fibers also demonstrated the potential for modulating complex optical devices. Based on the rectangular structure, Wang et al. [108] fabricated an acoustoelectric fiber, as shown in Fig. 3d. It can effectively detect underwater acoustic sources in the frequency range of 2–8 MHz, with a signal-to-noise ratio above 20 dB and the ability to demodulate multiple frequencies simultaneously. Additionally, a two-dimensional fiber array (Fig. 3e) was assembled, capable of locating underwater acoustic sources at the centimeter level.

Thermally drawn fibers have a micrometer-scale cross-sectional area. The small cross-sectional area makes them flexible and easy to assemble, but it also reduces the active area, thereby limiting the piezoelectric performance of the fibers. To increase the active area of acoustic fiber sensors, Chocat et al. [114] designed a folded structure, as shown in Fig. 3f, using P(VDF-TrFE) as the piezoelectric layer and PC as the insulating cladding. To resist capillary breakup while maintaining a certain level of conductivity, the electrodes were composed of low-viscosity carbon-loaded polyethylene (CPE) and BiSn. The uniformity of the fibers was

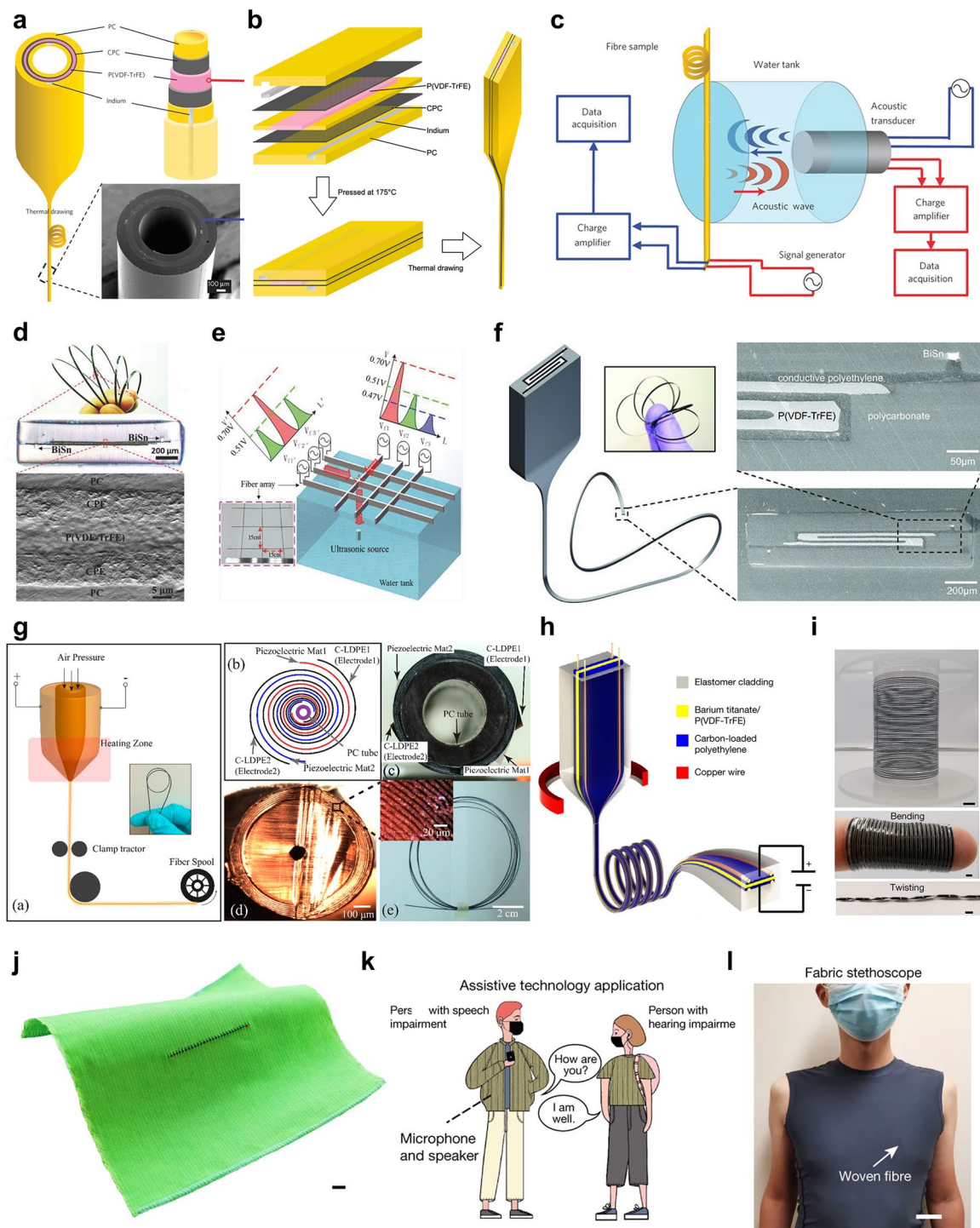


Fig. 3 Thermally drawn fibers for acoustic sensing. **a, b** Fabrication of cylindrical and rectangular acoustic fibers, both with the same material. **c** Experimental setup for acoustic characterization of acoustic fibers. Reproduced with permission [113] Copyright 2010 Springer. **d, e** Fabrication and acoustic sensor performance of piezoelectric fiber that can locate the source of hydroacoustic sound. Reproduced with permission [108] Copyright 2017 Wiley. **f** Fabrication of the acoustic fiber with a folded structure. Reproduced with permission [114] Copyright 2012 Wiley. **g** Fabrication of the acoustic fiber with a "Swiss roll" structure. Reproduced with permission [81] Copyright 2017 American Chemical Society. **h, i** Acoustic fiber with BTO/PVDF-TrFE composite as a piezoelectric layer. **j** Acoustic fabric containing a single piezoelectric fiber. **k, l** Applications in communication and heart rate detection. Reproduced with permission [19] Copyright 2022 Springer

demonstrated through multifiber interference experiments. The extensive contact area effectively enhanced the piezoelectric performance of the fibers, paving the way for acoustic sensors over large areas and even complex three-dimensional structures.

P(VDF-TrFE) can spontaneously crystallize into the β -phase during the drawing and solidification process, avoiding the complex polarization process. However, it is expensive. Additionally, the incorporation of metal electrodes in the studies above limits the flexibility of the fibers. To address these issues while enhancing the piezoelectric performance of the fibers, Lu et al. [81] innovatively fabricated a fiber with a "Swiss roll" structure. They used carbon-impregnated low-density polyethylene (C-LDPE) as the electrode layer and perovskite ceramic (BaTiO_3 or $\text{Pb}(\text{Zr}_{0.52}\text{Ti}_{0.48})\text{O}_3$) nanoparticles and carbon nanotubes (CNTs) into the PVDF layer, improving the piezoelectric performance while ensuring flexibility. The piezoelectric and electrode layers are alternately arranged to form a multilayer cladding, as shown in Fig. 3g. This structure further increases the piezoelectric material's active area and simplifies the fibers' connection. The square of the fiber's output voltage is proportional to the acoustic wave frequency, making it suitable for sound insulation detection.

The previous research only focused on acoustic fibers without weaving them into fabrics. There are two significant challenges in realizing sensitive acoustic fabrics. Traditional fabrics have the property of damping sound, and acoustic fibers have low sensitivity in the air. Inspired by the eardrum in the human auditory system, Yan et al. [19] innovated from both fiber and fabric levels and realized an acoustic fabric that relies solely on one single piezoelectric fiber. The piezoelectric fiber was fabricated via the thermal drawing process, and its structure is shown in Fig. 3h, i. The piezoelectric layer was composed of barium titanate and P(VDF-TrFE) composite. CPE and four copper wires together served as electrodes, which were asymmetrically encapsulated in the styrene-(ethylene-*co*-butylene)-*b*-styrene (SEBS) cladding. To enhance the sensitivity of the acoustic fiber, a stepwise polarization method was proposed, where 0 V and gradually increasing voltages were applied alternately. Eventually, the piezoelectric constant d_{31} of the fiber reached 46 pC/N. Moreover, a strong coupling between the fiber and the membrane's mechanical vibration mode led to higher electrical output than an individual fiber, further boosting sensitivity. The SEBS ensured the fiber's flexibility, allowing it to be

woven into the fabric using a traditional loom. As shown in Fig. 3j, the fabric has the same cotton warp and high-modulus Twaron filament yarns in the weft direction. The fabric exhibited excellent electrical signals within the audible frequency range. The volume of the fiber in the fabric is less than 0.1%. The fiber obtained from a single stretching process can be used to make a fabric covering dozens of square meters. It demonstrated superior performance to acoustic sensors fabricated via other methods [115], while achieving performance levels comparable to commercial microphones. Finally, the acoustic fabric was demonstrated in applications such as sound direction detection, acoustic communication, and heart rate detection (Fig. 3k, l). This scalable acoustic fabric holds promise for advancing the fields of human-computer interaction and physiological monitoring.

3.3 Mechanical Sensors

As a part of flexible electronics, mechanical fiber sensors are not only crucial for detecting various human movements but also key component in flexible robotics. Mechanical sensors mainly include the measurement of three types of deformation: pressure, strain, and bending. Mechanical TDFSs hold great potential in multiple fields, such as Morse code translation, chronic disease detection, smart fabrics, and ion concentration measurement.

The principles of TDFSs for pressure sensing mainly involve resistance and capacitance. The principle of capacitive pressure sensors is analogous to temperature sensors. Unlike temperature sensors, in resistive pressure sensors, the primary contributor to resistance change is the geometric deformation caused by applied pressure. Gorgutsa et al. [61] fabricated a pressure fiber sensor based on capacitance, marking the first attempt of the thermal drawing process in the field of mechanical sensors. The preform was rolled from two dielectric films and two conductive polymer films, forming a "Swiss roll" structure that significantly enhanced capacitance. A single fiber could achieve sliding sensing. However, it could only detect touch points closest to the external electrodes, limiting its applications. To address this issue, Nguyen-Dang et al. [116] developed a pressure fiber sensor with a cantilever structure based on microelectromechanical system (MEMS) (Fig. 4a). Two CPC electrodes with linear resistance were selected. When pressure was applied, two electrodes made partial contact, generating an

electrical signal. The signal was linearly correlated with the pressure position at a submillimeter resolution. This fiber could locate two simultaneously applied pressure points, making it the first 1D system capable of locating multiple pressure points without relying on a 2D network (Fig. 4b).

The PSU cladding of microelectromechanical fiber (MEMF) is rigid. With the development of flexible electronics, people are increasingly inclined to choose flexible and stretchable elastomeric materials to expand their applications in wearable devices. Despite more than a decade of research in thermal drawing, selecting an elastomeric cladding that maintains high viscosity during the drawing process remains a challenge. To address this issue, Qu et al. [72, 117] analyzed the rheological properties and microstructures of different materials and developed the rheological criteria of the thermal drawing process. They ultimately demonstrated that various thermoplastic elastomers (TPEs), such as geniomer and SEBS, have the potential to be used as claddings. For example, SEBS fibers can withstand up to 500% elastic deformation. By introducing two parallel liquid metal (LM) electrodes, as shown in Fig. 4c, the pressure was quantified for the first time based on the principles of resistance and capacitance, with a detection limit as low as 0.01N.

Researchers have conducted extensive studies based on TPEs. For example, Leber et al. [80] used SEBS as the cladding and CPE as the polymer electrode. By constructing an asymmetric structure shown in Fig. 4d, they fabricated a fiber sensor capable of simultaneously locating and quantifying pressure. Its signal response showed negligible variation after 10,000 loading–unloading cycles. The fiber, obtained by a single drawing process, was divided into eight strands and integrated into a gymnastics mat (Fig. 4e–g). They can accurately capture the body's position, posture, and movements. Compared to conventional 0D sensor networks, this approach significantly reduced the number of electrical connections. This fiber achieved large-area pressure sensing for the first time, but the pressure resolution was poor. Yu et al. [49] leveraged the high elasticity of TPEs and combined them with the FDR measurement method to preliminarily realize distributed pressure sensing. The fiber featured copper wires as the electrodes and PC as the cladding, with the structure shown in Fig. 4h. When subjected to multipoint pressure, the distance between the parallel copper wires changed, altering the fiber's impedance, which generated multiple reflection signals, thus enabling the precise location of multipoint pressure (Fig. 4i–k). The spatial resolution of the fiber was 2.2 cm, and the pressure

resolution was 4 kPa. Leber et al. [118] improved this method by combining the TDR measurement method to fabricate a pressure fiber sensor with liquid metal electrodes arranged coaxially (Fig. 4l). Compared to copper wire electrodes, liquid metal electrodes are more deformable (Fig. 4m, n), enhancing the pressure resolution to 0.2 N. When woven into fabric for testing (Fig. 4o), the fiber could accurately locate and quantify multiple pressure points with a spatial resolution of less than 1 cm. This method further reduced electrical connections, making it highly suitable for flexible wearable devices.

Conventional fiber structures only have sensing capabilities in specific directions. Although previous studies have investigated detecting the direction of pressure [72], isotropic pressure sensors have remained a challenge. Recently, Zhang et al. [79] have fabricated the helical two liquid metal channel SEBS fibers (HTLSFs) (Fig. 4p–r). The unique structure provides the fibers with over 1000% strain and excellent electrical conductivity, allowing them to sensitively respond to both small and dynamic pressures over a wide range. Furthermore, when pressure is applied in different directions, the change in fiber resistance is almost identical (Fig. 4s), extending the application scenarios of pressure TDFSs in complex environments.

The principles of TDFSs for strain sensing mainly involve resistance, capacitance, and photoelectricity. Only after the thermal drawing rheological criteria were proposed that researchers began studying strain sensors. By incorporating two parallel liquid metal electrodes into SEBS, a strain sensor was easily fabricated based on resistance and capacitance principles (Fig. 5a) [72]. Capacitive strain sensors have good linearity but small changes in capacitance. To improve the signal response amplitude, Leber et al. [73] used nanocomposites as electrodes to fabricate a fiber with a structure resembling an axial lead capacitor (Fig. 5b). This special structure increased the fiber's capacitance by 13 times compared to the standard parallel-plate structure. Figure 5c shows the current variation of the fiber with an elongation rate between 50 and 100%, demonstrating good strain sensing performance.

In addition, photoelectricity is also applied in strain sensors. By utilizing the difference in refractive indices of two types of SEBS, light loss under different deformations can be measured to detect strain changes [119]. As a type of TPE material, polyurethane (TPU) has self-healing properties after special treatment. Based on this, Qi et al. [82] proposed a structurally simple self-healing fiber. An original

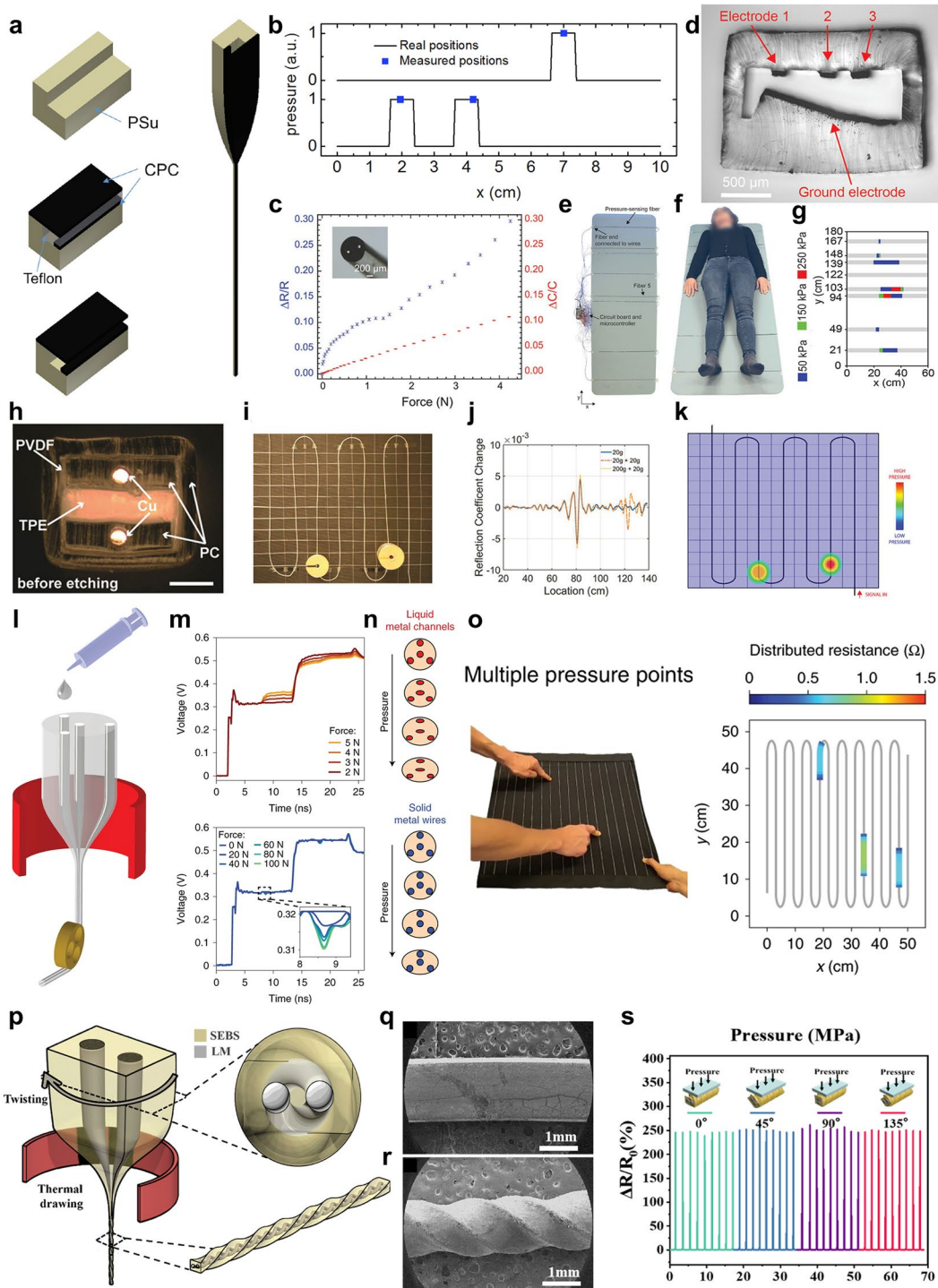


Fig. 4 Thermally drawn fibers for pressure sensing. **a** Fabrication of a MEMF. **b** Two-point pressure test. Reproduced with permission [116] Copyright 2017 IOP. **c** TDFS for pressure quantification. Reproduced with permission [72] Copyright 2018 Wiley. **d** Fiber for pressure quantification and location. **e–g** Eight pressure fiber sensors are integrated into a gymnastic mat for body posture and motion monitoring. Reproduced with permission [80] Copyright 2020 Wiley. **h** Optical microscopic image of FDR-based fiber cross section. **i–k** Physical image, reflection coefficient changes, and reconstruction of pressure map of multipoint pressure testing. Reproduced with permission [49] Copyright 2020 Wiley. **l** Fabrication of a TDR-based fiber. **m** Waveforms of liquid metal top and solid metal bottom triangular lines. **n** Schematic of the cross-sectional deformation mechanism of lines under increasing pressure. **o** Three-point pressure test. Reproduced with permission [118] Copyright 2020 Springer. **p–r** Fabrication and morphology of HTLSF. **s** Variation in relative resistance of HTLSF under the same pressure in different directions. Reproduced with permission [79] Copyright 2020 Chinese Society of Metals

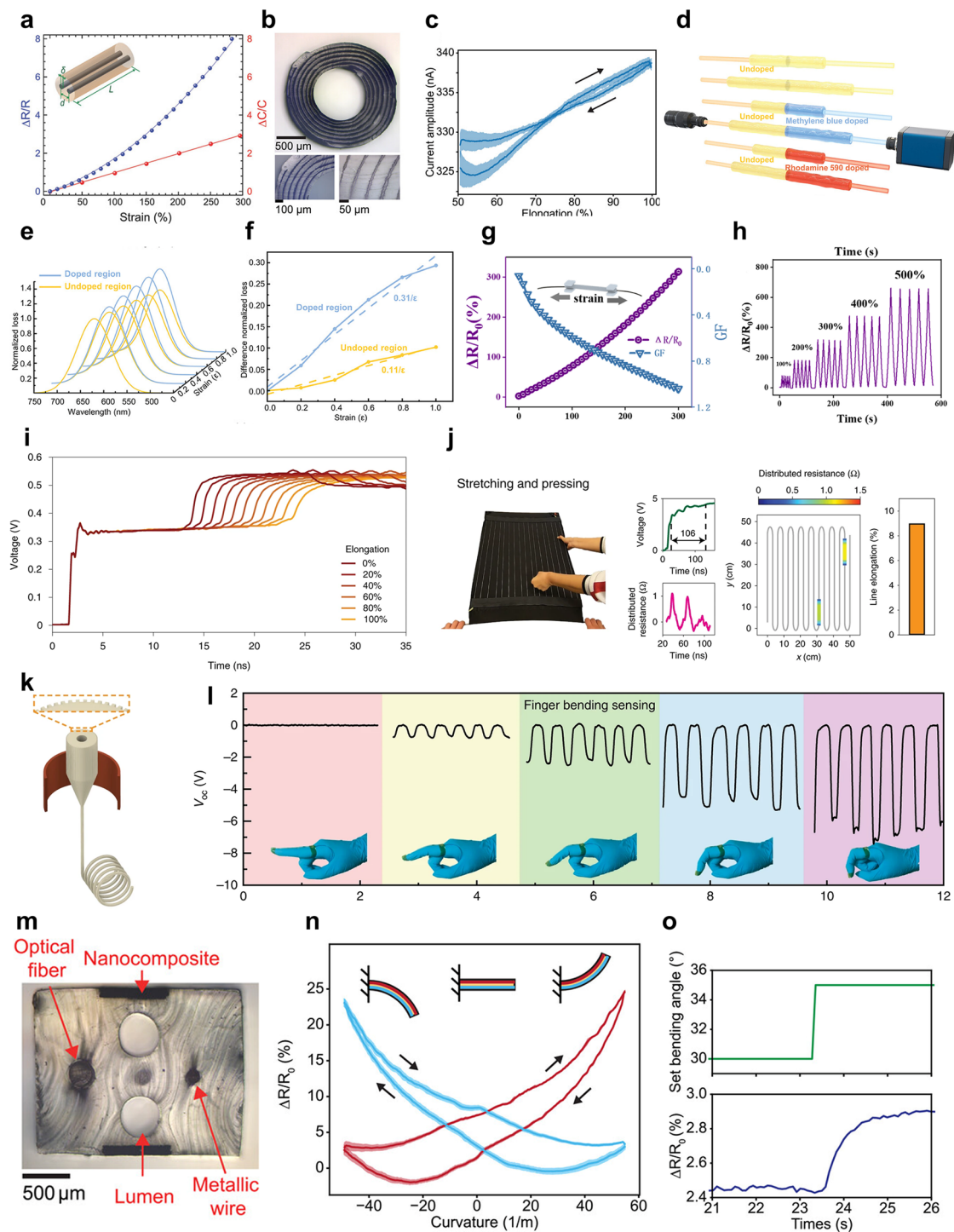


Fig. 5 Thermally drawn fibers for strain and bending sensing. **a** Structure and performance of resistive and capacitive strain sensors. Reproduced with permission [72] Copyright 2018, Wiley. **b, c** Optical image and strain sensing performance of a capacitive strain fiber sensor. Reproduced with permission [73] Copyright 2023 Wiley. **d** Schematic of the testing method for photoelectric strain sensors. **e, f** Normalized absorption spectra variation of the strain sensor and the difference normalized loss. Reproduced with permission [82] Copyright 2024 Wiley. **g** Variation in relative resistance and GF value of HTLSF with respect to tensile strain. **h** Relative resistance changes of HTLSF at different strains. Reproduced with permission [79] Copyright 2020 Chinese Society of Metals. **i** Waveform changes with elongation. **j** Simultaneous measurement of multipoint pressure and strain. Reproduced with permission [118] Copyright 2020 Springer. **k** Fabrication of a TENG fiber with micron-scale surface textures. **l** Finger bending sensors. Reproduced with permission [127] Copyright 2020 Springer. **m** Optical image of a fiber cross section, integrating two nanocomposite electrodes. **n** Relative resistance changes versus the fiber curvature for both nanocomposite electrodes. **o** Relative resistance changes of the nanocomposite to a small bending angle step of 5° . Reproduced with permission [73] Copyright 2023 Wiley

Table 4 Performance parameters of pressure sensors and strain sensors

Sensor types	Principles	Range	Sensitivity	Resolution	Spatial resolution	References
Pressure sensors	Resistance	–	0.3 N	–	0.75 mm	[116]
	Capacitance	> 5 N	20 mV N ⁻¹	0.2 N	< 1 cm	[118]
Strain sensors	Capacitance	100%	0.1 ns % ⁻¹	0.25%	–	[118]
	Photoelectricity	100%	0.31/ε	–	–	[82]

STPU fiber was spliced with a methylene blue-doped STPU fiber and tested in the device shown in Fig. 5d. As strain increased, the normalized loss of both fibers increased, with the methylene blue-doped fiber showing more significant changes (Fig. 5e, f). The fiber exhibited a nearly linear response across the 100% strain range, making it suitable for distributed strain sensing. Moreover, with the self-healing feature, the fiber is more durable, making it convenient for long-term application. The HTLSF introduced in the pressure sensing section can also be used as a strain sensor [79]. Compared to previous studies, its strain range has been increased to 500% (Fig. 5g, h). However, it cannot simultaneously measure strain and pressure. In the TDR-based fiber, as the elongation increases, the signal transmission time also increases, enabling strain sensing with a strain resolution of 0.25% (Fig. 5i). Additionally, by decoupling the reflection signals, simultaneous measurement of multipoint pressure and strain can be achieved [118] (Fig. 5j). This represents a groundbreaking breakthrough in mechanical sensing, providing a feasible solution for the application of multifunctional TDFSs in flexible wearable devices and robotics.

Table 4 summarizes the performance parameters of pressure and strain sensors based on different principles. Resistive pressure sensors exhibit a lower theoretical spatial resolution, but they cannot simultaneously detect more than two pressure points. Capacitive pressure sensors possess distributed sensing capabilities, yet they have a narrower measurement range. Capacitive and optical strain sensors demonstrate comparable performance but differ in applications. Capacitive strain sensors prove more cost-effective for large-scale distributed sensing, while optical strain sensing is better suited for non-contact measurement. In summary, thermally drawn pressure sensors show superior comprehensive performance compared to those fabricated by other methods [120]. However, the performance of strain sensors still require further improvement.

The principles of TDFSs for bending sensing mainly involve resistance and triboelectric nanogenerators (TEGs). TENGs convert mechanical energy into electrical energy through by coupling contact electrification and electrostatic induction [121]. When external stimuli are applied to a TENG, materials with different electron affinities contact, generating opposite charges. After the external force disappears, the materials separate, and electrons in the external circuit flow to balance the potential, generating an electrical signal. When external force is reapplied, electrons flow in the opposite direction. When the two materials come into contact again, the induced charges are neutralized, and there is no electron flow [122]. The voltage output formula of TENGs is as follows [123]:

$$V = -\frac{1}{C(X)}Q + V_{oc}(X) \quad (9)$$

In the formula, V is the total voltage, C is the capacitance, X is the distance between two electrodes, Q is the charge transferred between the electrodes, and V_{oc} is the contribution to the voltage from the polarized triboelectric charge. TENG has a wide range of material choices, a simple structure, low cost, and the ability to self-power, making them an ideal alternative to piezoelectric sensors [91, 124]. However, the sensing performance of TENGs is easily influenced by environmental factors, and they are only sensitive to dynamic pressure. Theoretically, materials with a greater difference in electron affinity generate a larger voltage [125, 126]. Additionally, altering the surface roughness of materials is another method to enhance voltage output.

Dong et al. [127] found that geniomers, as a TPE, also possess negative triboelectric polarity, making it suitable cladding for TENG fibers. Based on this, they integrated liquid metal electrodes and fabricated a TENG fiber with micron-scale surface textures (Fig. 5k). The fiber exhibited

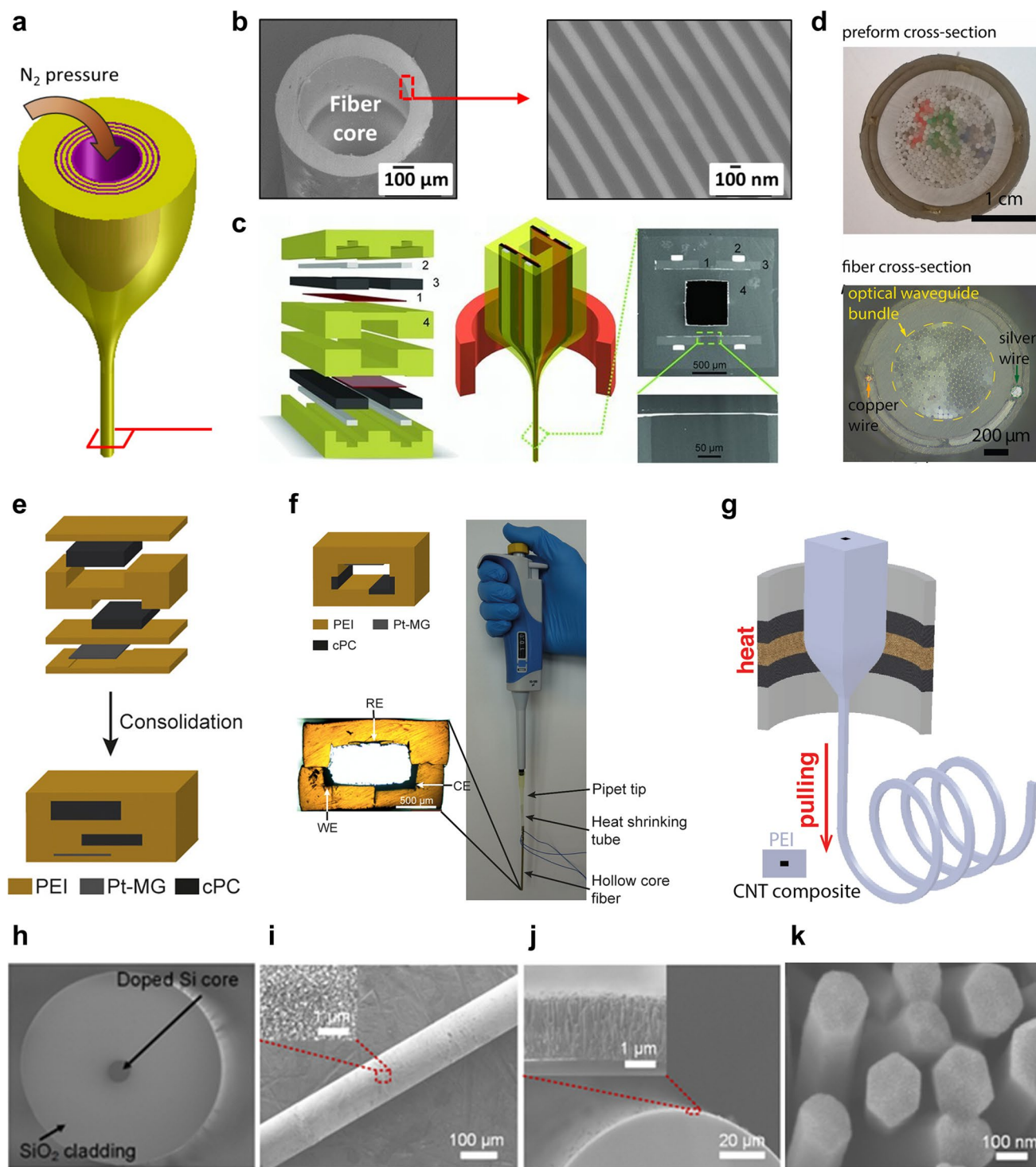


Fig. 6 Thermally drawn fibers for chemical sensing. **a, b** Fabrication and principle of the PBG fiber. Reproduced with permission [131] Copyright 2012 The Optical Society. **c** A completely distributed chemical sensor. Reproduced with permission [50] Copyright 2012 Wiley. **d** PH probe based on LAPS. Reproduced with permission [133] Copyright 2021 Elsevier. **e** Preform-making process of a three-electrode electrochemical sensor. **f** Cross section of the hollow core fiber. Reproduced with permission [83] Copyright 2021 American Chemical Society. **g** Fabrication of the CNT composite fiber. Reproduced with permission [134] Copyright 2019 Multidisciplinary Digital Publishing Institute. **h–k** SEM images of the Co-doped ZnO NRs chemical sensors. Reproduced with permission [135] Copyright 2023 American Association for the Advancement of Science

enhanced open-circuit voltage with operational stability over 40,000 cycles. When attached to a glove, the fiber's voltage output varied with the bending angle (Fig. 5l). The above research only roughly described how the fiber's voltage output changes with the bending angle, without quantification. Leber et al. [73] used nanocomposites as electrodes to fabricate a fiber with the structure shown in Fig. 5m. At different bending angles, the upper and lower electrodes are in stretching and compressing states, respectively, causing changes in resistance and enabling quantification of the bending angle (Fig. 5n). As shown in Fig. 5o, the fiber can detect bending changes as small as 5°. Overall, the development of bending sensors is still in its infancy. Their sensitivity, response time, and other performance aspects need to be improved.

3.4 Chemical Sensors

Based on specific sensing materials, chemical sensors enable qualitative and highly sensitive quantitative detection of target analytes, with broad applications spanning biomedical diagnostics, environmental monitoring, food safety, and hazardous substance detection [50, 83, 128, 129]. Thermal drawing process can form specific micro–nanostructures, providing a novel fabrication process for highly sensitive, low-cost miniaturized chemical sensors. Based on different signal transduction mechanisms, the chemical TDFSs developed so far can be divided into two categories: photochemical sensors and electrochemical sensors, each with unique detection capabilities and application potential.

Light is an effective form of noninvasive energy for sensing various stimuli. Currently, photochemical sensors mainly achieve sensing functions by detecting changes in light wavelength ($\Delta\lambda$). Photonic bandgap (PBG) fibers control the propagation of light by designing periodic structures with different refractive indices. Only light outside the bandgap within a specific wavelength range can be reflected [130]. Stolyarov et al. [131] combined the principles of chemiluminescent (CL) reactions and PBG fibers, fabricating a hollow multilayer PBG chemical fiber sensor (Fig. 6a, b). During the drawing process, external gas was introduced into the hollow fiber under controlled pressure to modulate the optical transmission bandgap, increase the core diameter, and reduce transmission loss. Meanwhile, the CL material was centrally placed inside

the fiber, enhancing detection sensitivity. The CL material reacted exclusively with hydrogen peroxide (H_2O_2) vapor, which avoided the influence of environmental factors on the experimental results. The minimum detectable concentration of H_2O_2 vapor by the sensor reached 100 ppb. However, limitations such as the fiber's numerical aperture, transmission, and bending loss restrict the detection distance and sensitivity of photochemical sensor. To overcome these drawbacks, Gumennik et al. [50] adopted a monolithic integration approach using Se_{97}S_3 as the CL material to achieve distributed chemical sensing along the entire fiber length. The preform (Fig. 6c) integrated two independent optical detection units distributed on either side of a rectangular hollow core, further improving detection sensitivity. Se_{97}S_3 also reacted exclusively with H_2O_2 , and its minimum detectable concentration for hydrogen peroxide is reduced to 10 ppb. This fiber sensor provides a concept for long-range and distributed sensing over hundreds of meters, with sensing capabilities comparable to films [132]. Overall, photochemical sensors exhibit high sensitivity, low signal transmission loss, and extremely low detection limits.

Electrochemical sensors are widely recognized for their simplicity in testing and low cost, making them particularly advantageous in quantitative analysis. Measuring pH *in vivo* has long been a challenge. Guo et al. [133] developed an integrated pH probe for spatial pH sensing (as shown in Fig. 6d) based on a light-addressable potentiometric sensor (LAPS). The Si_3N_4 sensing layer specifically responds only to H^+ ions, showing negligible interference from other ions (such as Na^+ , K^+). The fiber can simultaneously measure pH variations across 14 pixels without environmental interference, achieving a spatial resolution of 250 μm and a temporal resolution of 30 Hz. This novel label-free chemical sensor is significant for revealing the relationship between brain neural activity and pH changes.

Richard et al. [83] fabricated a three-electrode electrochemical fiber sensor. In the preform shown in Fig. 6e, $\text{Pt}_{57.5}\text{Cu}_{14.7}\text{Ni}_{5.3}\text{P}_{22.5}$ (Pt-MG) was used as a pseudo-reference electrode, and two carbon-black-filled conductive polycarbonate (cPC) films were used as working and counter electrodes. The cPC surfaces were chemically treated to enhance electrochemical activity. To further improve sensitivity, a capillary structure with a high surface area was fabricated (Fig. 6f). Using cyclic voltammetry (CV) or chronoamperometry (CA) for testing, the fiber exhibited



sensitivity comparable to commercial screen-printed electrodes (SPE), demonstrating its ability to detect acetaminophen. Furthermore, after functionalizing chemical sensors with different ion recognition elements, they can also quantify ion concentrations. For instance, inspired by nanocomposites, Nishimoto et al. [134] incorporated (CNTs) into carbon-black-impregnated polyethylene (CB-CPE) to fabricate a composite fiber (Fig. 6g). The high catalytic activity of CNTs enables them to preferentially catalyze the oxidation of dopamine (DA) at a fixed potential (0.6 V), while other interfering species exhibit low oxidation currents under this potential. By adjusting the CNTs content, they significantly improved the fiber's viscoelastic compatibility and electrochemical sensing performance. In vitro, the detection limit for DA reached as low as 10 nM. After functionalizing the fiber with ion-sensitive membranes (ISM), it could selectively monitor Na^+ concentrations. Additionally, by combining the principles of metal oxide semiconductor (MOS) sensors, gas detection is feasible. Niu et al. [135] in situ grew Co-doped ZnO nanorods on the surface of Si/SiO₂-doped fibers (Fig. 6h–k). Co doping reduced the operating temperature of ZnO and preferentially enhanced its selectivity toward CH₄. At 50 °C, the fiber achieved a maximum detection sensitivity of 16% for 1000 ppm CH₄. Integrated into miners' clothing, the sensor can monitor CH₄ concentrations in real time, ensuring safety in mines. Furthermore, Iwama et al. [58] combined a closed bipolar electrode (cBPE) array with the thermal drawing process to develop an electrochemical imaging system capable of 2D imaging of chemical signals within organisms. Overall, electrochemical sensor technology is relatively mature, offering the advantages of low cost and good stability.

3.5 Biosensors

Flexible biosensors are a crucial component in modern biomedical fields [136, 137]. Multifunctional thermally drawn fibers, with excellent flexibility, biocompatibility, and controllable dimensions, can minimize foreign body reactions, making them highly suitable for implantable and wearable biomedical devices [138, 139]. Among these, implantable neural probes, as key tools for studying neurological disorders, have garnered significant attention [140]. However, the elastic modulus of commonly used silicon-based materials is much higher than that of neural tissue. Over prolonged

use, this discrepancy can lead to a decline in the signal-to-noise ratio (SNR) and even neuronal damage, ultimately compromising the device's longevity [141–143] and hindering advancements in the field of flexible neural probes. Consequently, developing neural probes with high SNR, biocompatibility, and long-term stability holds profound significance.

With the development of fluorescence sensors and optogenetics [144, 145], using light-sensitive proteins (e.g., Channelrhodopsin-2), probes have enabled precise stimulation or inhibition of specific neuronal activities. Light has thus become the primary method for neural probe stimulation. To enhance biocompatibility and extend the life span of probes, two main solutions have emerged.

One solution is to fabricate probes entirely from flexible materials [146]. In 2015, Canales et al. [71] fabricated a neural probe that combined PC and conductive polyethylene (COC) to provide optical waveguides, with CPE as the polymer electrode. The probe also incorporated microfluidic channels, as illustrated in Fig. 7a. It can perform optogenetic stimulation, electrical neural recording, and drug delivery simultaneously. Tests on an adult mouse showed that the probe could operate stably for up to two months (Fig. 7b, c). In neural probes, extracellular electrophysiological recordings typically require electrodes with an impedance of less than 2 MΩ [139]. However, CPE electrodes exhibit poor conductivity. When meeting the impedance requirement, the electrode dimensions tend to be larger, which may induce foreign body reactions. Therefore, it is necessary to find highly conductive flexible electrodes to replace CPE. Park et al. [147] used a similar structure (Fig. 7d, e) and doped 5% graphite into the CPE (gCPE) to reduce impedance. The resulting neural probe had a diameter of less than 200 μm and a life span of three months. Figure 7f, g show the probe's functionality for viral delivery. Lu et al. [148] coated conductive silver nanowires (AgNWs) around the coaxial probe to enhance the conductivity of the probe. Although AgNWs don't belong to polymers, their incorporation maintains the probe's excellent flexibility. In tests in freely moving mice, the fibers could stimulate certain muscle groups, making them useful for research on neural pathways after spinal cord injury. CNTs, known for their excellent conductivity, biocompatibility, and electrochemical properties, have been widely studied since their discovery [149–151]. Jeon et al. [84] initially thermally drew PC and PMMA coaxial fiber to provide optical waveguides and then wrapped the forest-drawn CNT sheets around the fibers (Fig. 7h). The neatly aligned

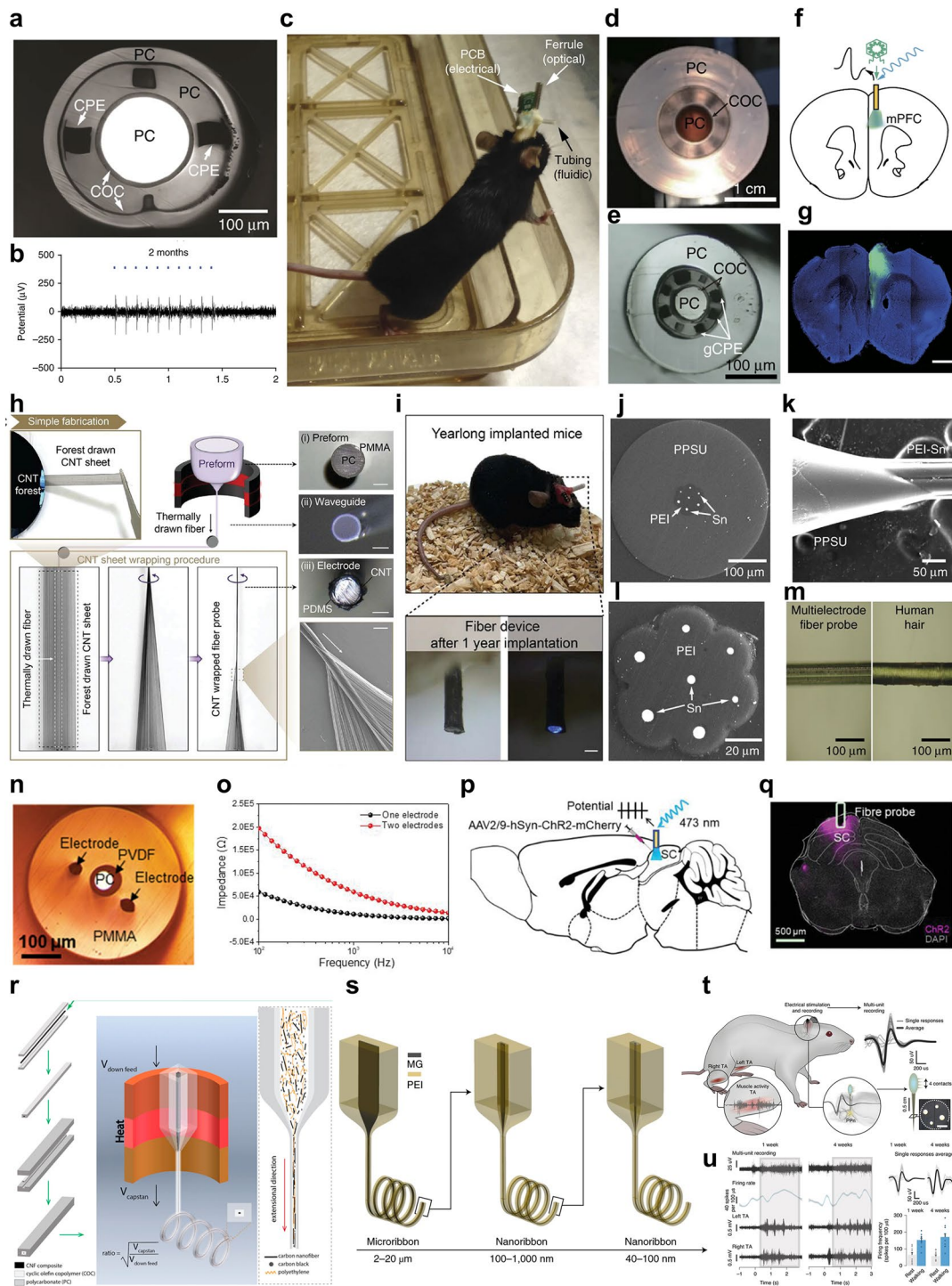


Fig. 7 Thermally drawn fibers for biosensors. **a** The cross-sectional image of the multimodality fiber. **b** Electrophysiological recording status after two months. **c** Multimodality fibers were implanted into mice. Reproduced with permission [71] Copyright 2015 Springer. **d, e** Cross-sectional images of the preform and the multimodal fiber with gCPE electrodes. **f, g** Schematic of viral delivery via the probe. Reproduced with permission [147] Copyright 2017 Springer. **h** Fabrication of the SAMP. **i** The image of the SAMP implanted mice for one year. Reproduced with permission [84] Copyright 2024 Wiley. **j** The SEM cross-sectional image of a multi-electrode probe. **k–m** After etching PPSU, the multi-electrode probe has a diameter of approximately 85 μm . Reproduced with permission [71] Copyright 2015 Springer. **n** The image of a fiber with two metal electrodes. **o** Impedance of different electrodes in fiber. **p, q** The image of the probe implanted into the SC. Reproduced with permission [153] Copyright 2020 Wiley. **r** Fabrication of the composite fiber. Reproduced with permission [85] Copyright 2021 American Chemical Society. **s** Fabrication of a nanoscale ribbon via multistep drawing. **t, u** Applications of electrical stimulation and recording based on MG fibers. Reproduced with permission [51] Copyright 2022 Springer

CNT sheets ensured excellent electrical signal recording. This structurally aligned multifunctional neural probe (SAMP) solved the problem of co-drawing high-conductivity electrodes with polymer. Moreover, the probes maintained stable function for up to one year (Fig. 7i), marking an unprecedented breakthrough in thermally drawn neural probes and surpassing most implantable probes [152].

Metal electrodes exhibit excellent conductivity but suffer from a large elastic modulus, poor flexibility, and low biocompatibility. Additionally, they typically have a high T_m , making it difficult to integrate with a polymer with low light transmission loss [138]. Therefore, a second solution has emerged, focusing on low T_m metal electrodes while minimizing electrode dimensions.

Canales et al. [71] used PEI as the cladding and fabricated polymer–metal multielectrode fiber probes through a two-step thermal drawing process. The diameter of the Sn electrode was reduced to 5 μm (Fig. 7j). After selectively etching polyphenylene sulfone resins (PPSU), the fiber size was reduced to 85 μm (Fig. 7k–m). Compared to conventional microwire electrodes, the smaller multielectrode probe induced fewer foreign body reactions, exhibited better biocompatibility, and had a life span of up to three months. Du et al. [153] designed a double-clad waveguide structure using PVDF and PMMA to improve the probe’s optical transmission performance (Fig. 7n). Two metal wire electrodes significantly reduced the impedance (Fig. 7o). Figure 7p, q shows a schematic of neural probe implantation into the superior colliculus (SC). The unique material and design enabled long-term (at least 10 weeks) simultaneous optical stimulation and neural signal recording with a high signal-to-noise ratio (SNR = 30 dB). Additionally, low-melting-point indium (In) can also be co-drawn with polymer [154]. A probe

incorporating three In electrodes has been demonstrated to be compatible with magnetic resonance imaging (MRI), enabling real-time visualization of brain fluid dynamics. Table 5 summarizes representative works of the two strategies from the perspectives of material selection, size, and service life.

Neural probes can also control neuronal activity through electrical signals [155]. To improve biocompatibility and life span, electrical stimulation neural probes also need to enhance flexibility and reduce size. By doping CPE with 2% CNFs, which align in situ during thermal drawing (Fig. 7r), the conductivity of the electrode is further improved. The size of the neural probe is reduced to less than 100 $\mu\text{m} \times 100 \mu\text{m}$, and the recording sites are comparable in size to individual neurons [85]. This microelectrode fiber can record high-quality neural activity from neurons near the electrode during long-term implantation, making them suitable for chronic electrophysiological studies and neurorehabilitation applications.

Metallic glass (MG), as an amorphous metal material, can better balance conductivity and size, along with high chemical stability and oxidation resistance, making it particularly advantageous for neural probes. Yan et al. [51] achieved the controlled fabrication of uniformly ordered MG fibers through multiple thermal drawing steps, reducing the size to approximately 40 nm (Fig. 7s). They further validated the feasibility of this size using principles of fluid dynamics. On this basis, they created probes with four MG electrodes embedded in PEI, enabling stable electrical stimulation and neural activity recording (Fig. 7t, u). This material provides a new approach to enhancing the life span of multimodal neural probes. Additionally, probes fabricated by combining the thermal drawing process and femtosecond laser

Table 5 Summary of the thermally drawn optogenetic stimulation neural probes

Optical waveguides		Electrodes		Size	Service life	References
Material	Loss	Material	Impedance			
<i>Polymer electrodes</i>						
PC/COC	2.7 dB cm^{-1}	CPE	0.5–2.5 M Ω	d = 400 μm	2 months	[71]
PC/COC	1.5 dB cm^{-1}	gCPE	0.62 \pm 0.23 M Ω	d = 180–220 μm	3 months	[147]
PC/PMMA	0.769 dB cm^{-1}	CNT sheet	0.22 M Ω	d = 160 μm	1 year	[84]
<i>Metal Electrodes</i>						
–	–	Sn	0.9 M Ω	d = 85 μm	3 months	[71]
PC/PVDF	1.18 dB cm^{-1}	Pt/Au/Cu	22.71 M $\Omega \text{ cm}^{-2}$	d = 200 μm	10 weeks	[153]

micromachining technology can achieve electroporation, showing potential for deep brain applications [156].

Overall, improving the biocompatibility of implantable neural probes is a key research focus in the field of biosensors, and the most crucial metric for measuring biocompatibility is the service life. Utilizing polymer materials and

reducing electrode size while meeting impedance requirements is an effective way to minimize foreign body reactions and extend the service life. Currently, a service life of up to one year can already meet the needs of many applications [84]. However, for use in the human body, it is necessary to

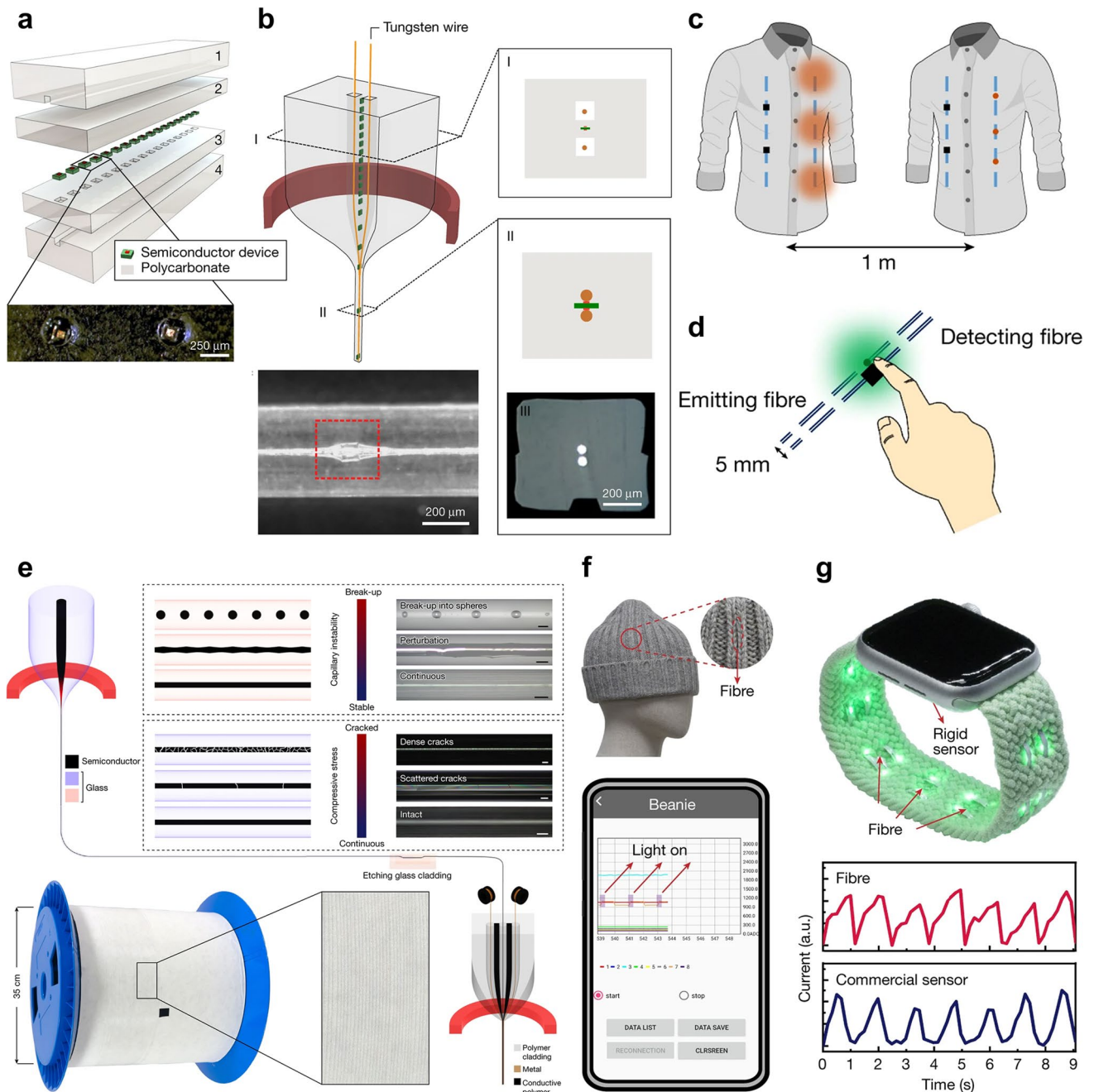


Fig. 8 Thermally drawn fibers for Optoelectronic sensing. **a, b** Fabrication of the diode fiber. **c** Schematic of the optical communication. **d** Application for heart rate detection. Reproduced with permission [43] Copyright 2018 Springer. **e** Fabrication of the semiconductor optoelectronic fiber. **f, g** Optoelectronic fabrics for ambient light detection and heart rate monitoring. Reproduced with permission [87] Copyright 2024 Springer

search for materials with even higher biocompatibility to further increase the upper limit of the service life.

In addition to implantable neural probes, thermally drawn fiber biosensors can also detect cell concentrations. Kanik et al. [86], combining microfluidic technology and TENG, fabricated a hollow PVDF fiber. By utilizing liquid for continuous medium exchange, the fiber not only achieved self-powering but also enabled biochemical analysis, allowing for the quantitative detection of ethanol and *Escherichia coli* cell concentrations. In the future, this innovation holds promise for expanding the range of detectable cells and advancing research in self-powered biosensors.

3.6 Optoelectronic Sensors

Optoelectronic sensors convert optical signals into electrical signals through photosensitive elements and can be used in fields such as ambient light detection and optical imaging. Semiconductors serve as the core material in these devices [25, 157, 158]. Among various semiconductors, glass semiconductors with low drawing temperatures and controllable fluid behavior are more compatible with common cladding and thus widely used in thermally drawn fibers [28, 159, 160]. However, their inferior electrical performance and damage resistance have limited the development of thermally drawn optoelectronic sensors, which will not be discussed here. This section will only introduce two fibers that can effectively improve the performance of thermally drawn optoelectronic sensors.

In 2018, Rein et al. [43] left grooves at fixed intervals in the preform to place semiconducting diodes (Fig. 8a). During the drawing process, the diodes separated axially, and the metal wire electrodes contracted transversely until they established electrical contact with the diodes (Fig. 8b). This method only altered their relative positions without changing their dimensions. By integrating light-emitting and photodetecting p-i-n diodes using this method, light-emitting fiber and photodetecting fiber were fabricated. The fiber exhibited optical detection abilities similar to the internal diodes. Its performance was enhanced by several orders of magnitude compared to photodetectors based on chalcogenide semiconductors. Furthermore, the fiber can be woven into fabrics and maintain stability even after several machine washes. By weaving light-emitting fiber and photodetecting fiber into two fabrics spaced a meter apart, optical communication

functionality was achieved (Fig. 8c). Additionally, the fibers can detect heart rate (Fig. 8d). This pioneering method further improves the device integration and functionality diversity in thermally drawn fibers, demonstrating the development potential of the "Moore's law for fibers."

In addition to directly integrating diodes, analyzing the thermal drawing criteria of crystalline semiconductors such as Si and Ge and finding suitable materials and methods are also significant for improving the performance of thermally drawn optoelectronic sensors. Recently, Wang et al. [87] have deeply analyzed the potential issues during the thermal drawing of Si and Ge, including cracks and fractures caused by residual stress, capillary instability phenomena, and so on (Fig. 8e). They attributed the causes to the mismatch of the thermal expansion coefficients between the glass cladding and the semiconductor core. To achieve a stable drawing of Ge semiconductor fibers, they replaced the SiO₂ cladding with aluminosilicate glass (ASG), which has an annealing point and a thermal expansion coefficient closer to Ge. With this material improvement, ultra-long, continuous, and fracture-free semiconductor fibers were achieved in a single thermal drawing step. The semiconductor fibers with removed cladding were further drawn with metal wires, conductive polymers, and insulating polymers into optoelectronic fibers with single-core and double-core structures. The fibers exhibited performance comparable to commercial planar optoelectronic sensors and excellent flexibility. After being woven into fabrics, they can be applied in various fields, such as ambient light detection and heart rate monitoring (Fig. 8f, g). This study provides a fundamental explanation of the fluid dynamics principles behind thermally drawn semiconductor fibers and advances the development of semiconductor materials in flexible sensors.

3.7 Other Emerging TDFSs

Thermal drawing process is an emerging large-scale fiber fabrication process, and many types of TDFSs are still in their early development. This section provides a brief overview of TDFSs for flow, magnetic, and humidity sensing, which have relatively less research, offering some guidance for researchers who wish to work in these fields.

Flow sensors, capable of locating fluid positions and analyzing flow rates, are critical components in clinical medicine, drug delivery, and environmental monitoring [161–163]. Their sensing principles include thermal flow,

capacitance, and TENG [164–166]. Among various principles, thermal flow sensor offers advantages in sensitivity, measurement range, and power consumption. However, its sensitivity, pressure drop, temperature rise, and measurement range influence each other, making it challenging to improve overall performance. To address this, Chen et al. [167] drew CPE, a conductive polymer with both high resistivity and large TCR, into hot films (Fig. 9a–d). The resulting fiber sensor maintained a flow velocity sensitivity of $384 \text{ mV min } \mu\text{L}^{-1}$ while keeping the maximum temperature rise to only $20 \text{ }^\circ\text{C}$, which is 5–10 times lower than typical MEMS sensors. Additionally, a multisegment structure was designed to enable high-resolution flow velocity detection within the range of 5–200 $\mu\text{L min}^{-1}$ (Fig. 9e, f). Although thermal flow sensors have a slight advantage in measuring varying flow velocities, they have some drawbacks. For instance, to avoid impurities affecting measurement accuracy, the fluid medium is ideally a pure liquid, and inevitable thermal losses can also affect the measurement results, limiting the detection of low flow rates. To overcome these limitations, Dong et al. [52] developed a microflow sensor based on capacitance. The fiber is hollow, with two CPE electrodes embedded in the PC cladding to provide capacitive signals (Fig. 9g–k). The sensor not only detected the position of the front fluid but also expanded the flow velocity range to 50 nL min^{-1} – 10 mL min^{-1} (Fig. 9l, m) and can even estimate the liquid concentration. Such a simple and scalable fiber sensor is crucial for detecting fluid signals in biomedical applications.

Magnetic sensors can detect magnetic field strength and direction, enabling the localization of object positions [168]. Due to the spatial distribution characteristics of magnetic fields, magnetic sensors are widely used in non-contact detection platforms [169]. In magnetic sensors, magnetic electronic components play a crucial role. Nitrogen vacancy (NV) quantum magnetometers, as one of these components, demonstrate unique advantages in magnetic sensing due to their spin-based quantum properties [170]. However, integrating optical, microwave, and magnetic excitation in a single system presented challenges, which limited the application of NV-based distributed sensing. Maayani et al. [171] addressed this issue through a two-step thermal drawing process. First, they fabricated a hollow silicon

fiber by high-temperature drawing, allowing the incorporation of NV-containing diamond liquid. Afterward, a polymer coating was applied to protect the fiber. This fiber was then drawn along with multiple photodiodes (PDs), copper wires, and PC cladding (Fig. 9n). Finally, the composite fiber was embedded in a larger coaxial cable for microwave (MW) excitation. The resulting distributed magnetic sensor achieved high-sensitivity magnetic measurements over a 90-m range with 102 monitoring points, each exhibiting a sensitivity of $63 \pm 5 \text{ nTHz}^{-1/2}$. The sensor also maintained stability in underwater tests (Fig. 9o, p). This fiber is expected to drive new applications for non-contact remote sensing in ferrous metal detection and biomedical fields.

Humidity, representing the amount of water vapor in the air, is a critical environmental parameter. Humidity sensors typically measure relative humidity (RH) and are widely used in environmental monitoring, industrial production, and medical fields [172–174]. However, the challenge of integrating thermal drawing processes to achieve flexible humidity sensors with both scalability and excellent sensing performance has persisted. So far, only one capacitive humidity fiber sensor has been fabricated. Tousi et al. [53] selected porous PEI as the sensing material, copper wires as the electrodes, and PPSU as the cladding to fabricate the preform (Fig. 9q). After drawing, the cladding was physically removed. The humidity tests were conducted in the device shown in Fig. 9r. The polymer's dielectric constant changed linearly with increasing moisture absorption, but its sensitivity was relatively low. To enhance performance, by controlling the water content of the preform and the cooling rate during the thermal drawing process, they fabricated an in situ porous structure in the PEI. Combined with capillary condensation phenomena [175], the sensor achieved a sensitivity of 0.39 pF/\% RH at higher RH levels (70%–80%) (Fig. 9s). Additionally, the sensor exhibited low-temperature dependency and excellent cycling stability. In the future, further improvements in various performance of humidity sensors are expected.

3.8 Multifunctional Sensors

With the development of flexible electronics, improving integration and expanding functionality diversity have become



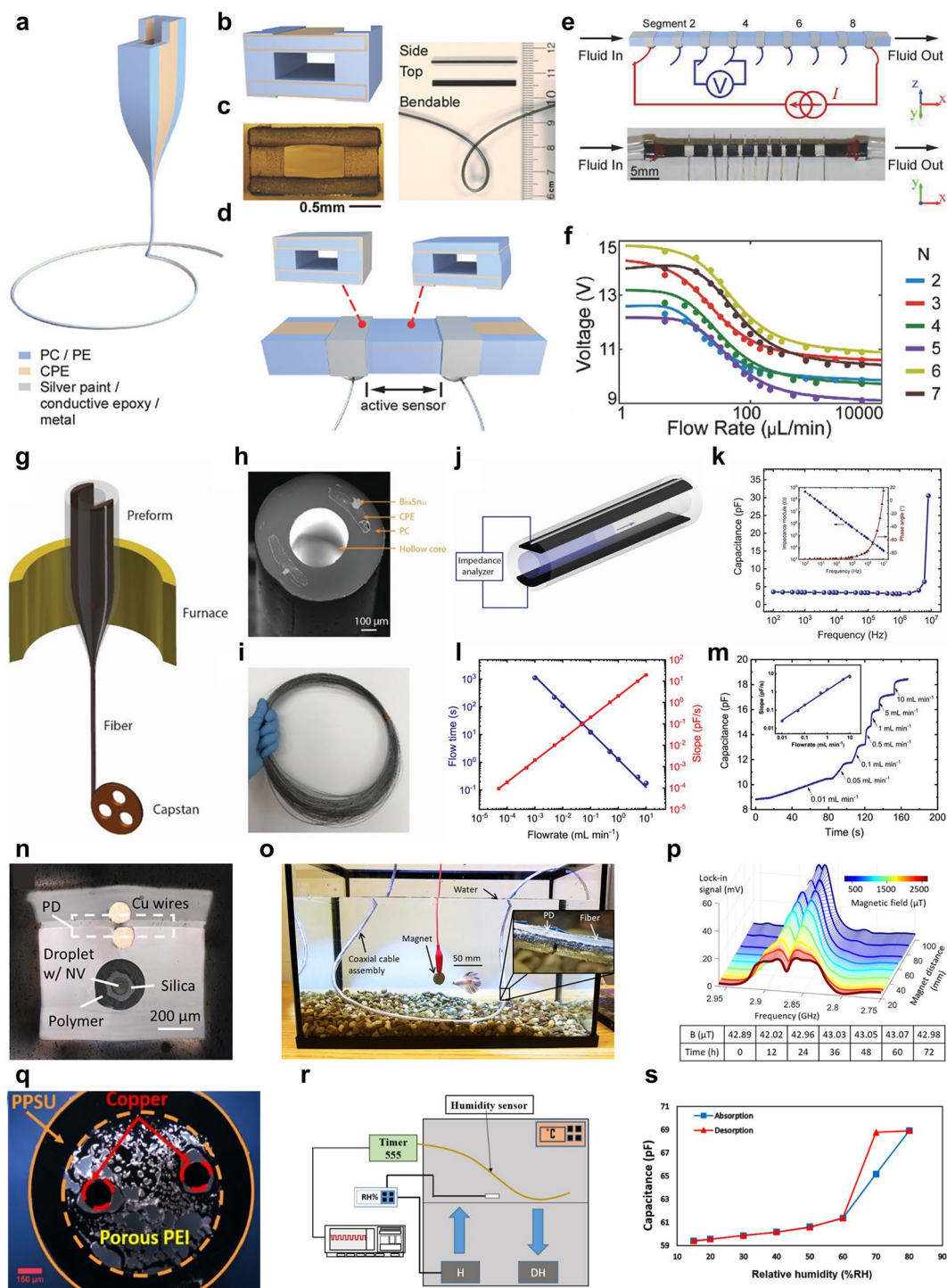


Fig. 9 Thermally drawn fibers for flow, magnetic and humidity sensing. **a–d** Fabrication of a flow fiber sensor. **e, f** Schematic of eight-segment fiber sensor flow test. Reproduced with permission [167] Copyright 2018 Wiley. **g–i** Fabrication of a capacitive flow sensor. **j, k** Capacitive performance of the fiber. **l, m** Flowrate detection of the fiber. Reproduced with permission [52] Copyright 2019 Wiley. **n** The cross-sectional image of the magnetic sensor. **o, p** Underwater magnetometry testing. Reproduced with permission [171] Copyright 2019 Wiley. **q** The cross-sectional image of the humidity sensor. **r** Schematic of the humidity measurement device. **s** Capacitance changes under different RH. Reproduced with permission [53] Copyright 2019 Multidisciplinary Digital Publishing Institute

key trends in the future. Researches on highly integrated and highly sensitive multiresponse sensors are becoming increasingly urgent [176]. Currently, various methods, such as wet spinning, chemical vapor deposition, and spin coating, have been applied in multifunctional sensors [177–179]. The thermal drawing process can produce nanometer-scale fibers with complex geometries and integrated multiple functions, making it a promising multifunctional sensing process [45]. However, at present, thermally drawn fiber-based multifunctional sensors are still in their infancy, with only a few studies conducted.

Chen et al. [180] developed a multifunctional fiber sensor based on TENG and electrochemical principles that can monitor contact positions and changes in ion concentration. They used a soluble-core method to fabricate hollow SEBS fibers (Fig. 10a), followed by the infusion of liquid metal electrodes into the hollow fibers. This approach circumvented the viscosity limitations imposed by thermal drawing, thereby expanding the range of material choices. This fiber, with superior flexibility and stretchability, can be applied on complex surfaces. For example, when integrated into a baseball glove, the fiber sensing network can three-dimensionally locate contact positions and estimate contact speed based on the magnitude of electrical signals (Fig. 10b, c). The fiber can also be integrated into a three-electrode electrochemical system as a conductive pathway (as shown in Fig. 10d). By applying an external voltage, the ion migration in the solution lead to changes in the internal current of the fiber. Combining its waterproof and easily encapsulated characteristics, the fiber can be utilized for undersea detection to sense changes in ion concentration.

Sahasrabudhe et al. [76] integrated multiple μ LEDs, electrodes, and microfluidic channels to fabricate a neural probe that can detect temperature as well as transmit and record physiological signals (Fig. 10e–h). The μ LEDs were key components of the probe, enabling easy temperature sensing due to the linear temperature dependence of resistance. They also served as light sources to apply optogenetic stimulation. The probe was first applied to the complex-shaped intestine. Furthermore, by coupling with the NeuroStack module, the probe enabled real-time wireless control of sensory epithelial cells and data transmission, overcoming several limitations of wireless bioelectronics. This probe provides crucial

information for establishing bidirectional communication between organs such as the intestines and the brain.

Recently, Gupta et al. [181] have fabricated a single-fiber computer integrating multiple sensing, storage, processing, and communication functions. The fiber used a foldable interposer method to map the two-dimensional layout of planar microdevices to a three-dimensional fiber structure, combined with helical copper wires and an elastic polymer cladding (Fig. 10i), endowing the fiber with a stretchability of over 60% and washability. Each fiber integrated a 32-bit floating-point microcontroller (MCU) and four multimodal sensors (a photodetector, a temperature sensor, a photoplethysmography (PPG) sensor, and an accelerometer) (Fig. 10j, k) and achieved distributed data processing via the I2C bus. Based on a wireless communication scheme, embedding four fibers into the clothing of the four limbs can realize physical activity prediction with a probability of 95%. This fully demonstrates the advantages of a distributed multifunctional sensing network.

In general, leveraging the unique advantages of thermal drawing process to integrate multiple commercial microsensors into fibers represents an effective approach to achieving multifunctional sensing. In the future, with the integration of the "Moore's law for fibers" [43], there will be a greater variety, higher density, and enhanced stability of microdevices that can be integrated into fibers. Consequently, thermally drawn fiber-based multifunctional sensors will become more ubiquitous.

4 Conclusions and Outlook

In recent years, thermally drawn fiber sensors have advanced rapidly. TDFSs integrate a variety of materials, including metals, semiconductors, and polymers, and cover multiple sensing principles such as resistance, capacitance, piezoelectricity, triboelectricity, photoelectricity, and thermoelectricity. These sensors achieve a wide range of sensing functions for temperature, acoustic, mechanical, chemical, biological, optoelectronic, flow, magnetic, and humidity sensing. Here, we summarize some challenges that TDFSs still faces and the potential development directions in the future.

Material: Recently, the variety of materials integrated into TDFSs has been increasing. Liquid metal electrodes, which

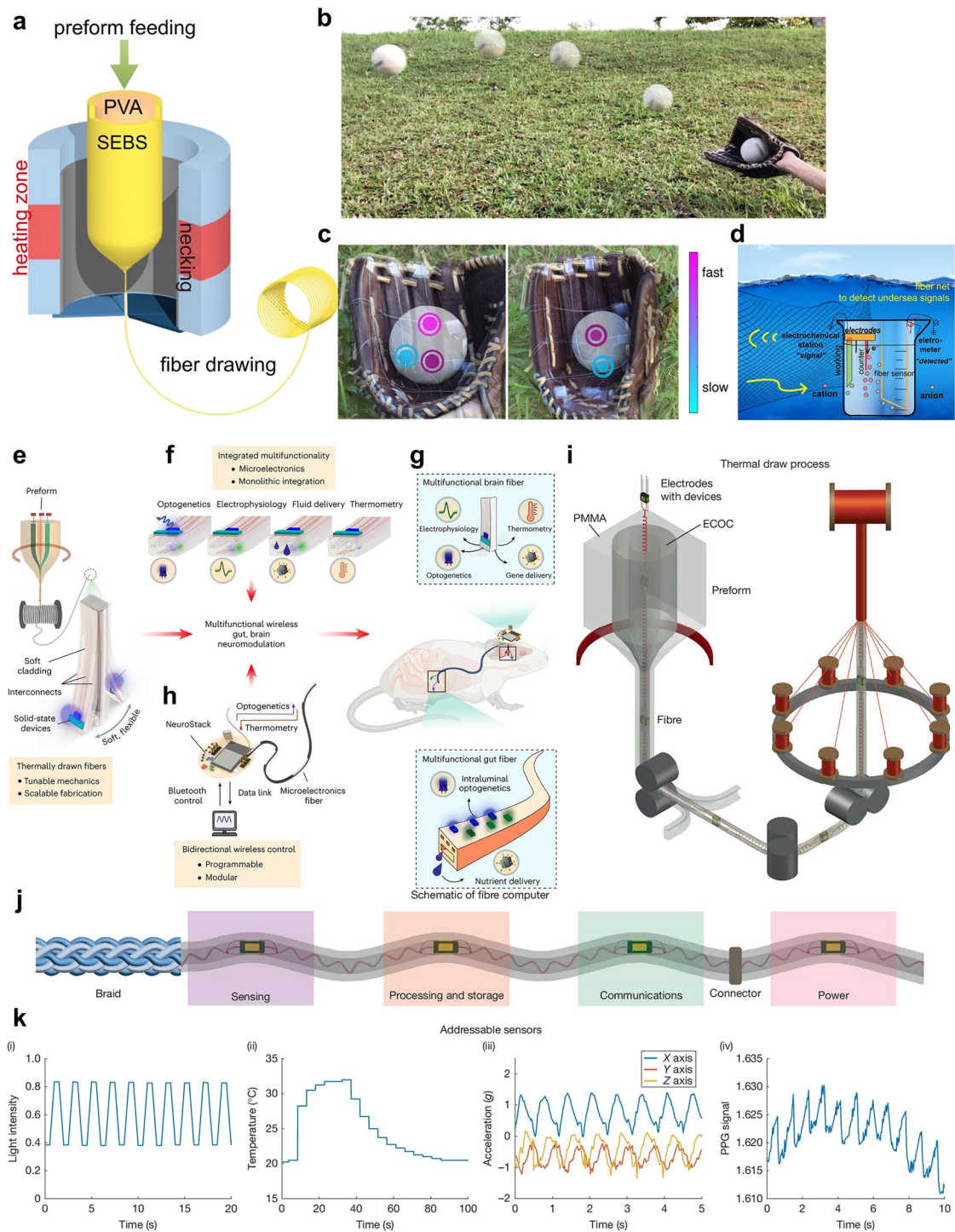


Fig. 10 Thermally drawn fibers for multifunctional sensing. **a** Fabrication of a mechanical and ion concentration sensor. **b, c** Application as a mechanical sensor. **d** Fiber for ion movement detection. Reproduced with permission [180] Copyright 2021 Springer. **e–h** Images of microelectronics-integrated multifunctional fiber that enable temperature and biological sensing. Reproduced with permission [76] Copyright 2024 Springer. **i** Fabrication of a fiber computer. **j** The image of a fiber computer incorporating diverse embedded devices. **k** Characteristic time series plots obtained from four sensors. Reproduced with permission [181] Copyright 2025 Springer

are more deformable, have shown great compatibility with the thermal drawing process and have been widely studied. Furthermore, with the introduction of rheological criteria, many of TPEs have emerged as viable options for function materials and cladding. Additionally, innovative methods have been developed to draw materials previously incompatible with the thermal drawing process. Therefore, it is urgent to establish a comprehensive material library that compiles various parameters of materials meeting the selection criteria. This would facilitate the initial material selection for researchers and accelerate the research and development cycle.

Structure: Fiber structure determines its applications. Over the past decades, to enhance performance, researchers have made multiple improvements to the structure. The preform structure has evolved from basic rectangular/circular structures [113] to multilayer folding structure [101, 162], and further to "Swiss roll" structure [56, 72]. These advancements have significantly increased the contact area and improved the performance of TDFSs. From the perspective of fiber microstructure, the emergence of techniques such as surface textures [127], direct imprinting technology [41], and double-helical structures of liquid metal electrodes [79] represents the development of thermally drawn fibers toward diversified structures and functionalities. However, currently, there is limited understanding of the microstructure-forming mechanism of thermally drawn fibers and the relationship between microstructure and functionalities. Therefore, it is necessary to focus on the microstructure and intensify research on the microstructure-forming mechanism of TDFSs to provide a foundation for performance enhancement.

Fabrication: The thermal drawing process exhibits excellent technological compatibility. It has been successfully integrated with techniques such as lithography and 3D printing. Additionally, multiple drawing steps can effectively reduce fiber sizes to meet application requirements. However, in actual fabrication, fractures and cracks remain the most challenging issues to address. Proper material selection and structure can mitigate these problems to a certain extent. Furthermore, various post-processing techniques are also meant to reduce residual stresses within fibers. Looking ahead, further diversification of post-processing techniques could pave the way for stable large-scale production of high-performance TDFSs.

Function: Currently, although TDFSs achieve diverse functions, most are concentrated in the single-sensing field.

With the advancement of flexible electronics, high integration and miniaturization of devices are certainly the trends. The research on composite sensors will surely be a crucial part of the trends. Current sensors often struggle to detect multiple stimuli simultaneously. Integrating microelectronic devices into fibers is one possible approach. However, in order to simplify structure and reduce size, decoupling multiple response signals within composite sensors remains a pressing challenge to be solved.

Stability: For sensors applied in flexible smart textiles, the long-term stability and chemical stability of the materials are critical factors. However, most researchers have not thoroughly investigated these aspects. Therefore, it is imperative to conduct in-depth analyses of failure mechanisms in TDFSs under complex environments after prolonged operation, ensuring the long-term mechanical stability and chemical durability of TDFSs.

As a prominent branch of flexible electronics and intelligent sensing, TDFSs will see substantial improvements in material diversity, structural customization, process stability, and functional integration. Moreover, in the context of interdisciplinary development, the deep integration of large-scale fabricated TDFSs with flexible e-skin and smart textiles will revolutionize the design logic of human-machine interaction interfaces. When synergized with deep learning algorithms, this convergence will enable more accurate and convenient recognition and prediction of diverse human physiological signals. TDFSs represent a highly promising class of flexible sensors, destined to become seamlessly integrated into daily life and propel technological innovations across diverse fields such as intelligent robotics and biomedical engineering.

Acknowledgements This work was supported by the National Key Research and Development Program of China (2023YFB3809800), the National Natural Science Foundation of China (52172249, 52525601), the Chinese Academy of Sciences Talents Program (E2290701), the Jiangsu Province Talents Program (JSSCRC2023545), and the Special Fund Project of Carbon Peaking Carbon Neutrality Science and Technology Innovation of Jiangsu Province (BE2022011).

Author Contributions ZZ was responsible for methodology, investigation, and writing original draft. YX took part in writing—reviewing and editing. PZ carried out investigation and data curation. XY was involved in investigation and conceptualization. CW assisted with methodology and data curation. XY participated in supervision and writing—reviewing and editing. HC contributed to project administration and funding acquisition. XZ was responsible

for supervision and funding acquisition. XW helped with supervision, methodology, and investigation. TZ took part in writing—reviewing and editing, supervision, and funding acquisition.

Declarations

Conflict of interest The authors declare no interest conflict. They have no known competing financial interests or personal relationships that could have appeared to influence the work reported in this paper.

Open Access This article is licensed under a Creative Commons Attribution 4.0 International License, which permits use, sharing, adaptation, distribution and reproduction in any medium or format, as long as you give appropriate credit to the original author(s) and the source, provide a link to the Creative Commons licence, and indicate if changes were made. The images or other third party material in this article are included in the article's Creative Commons licence, unless indicated otherwise in a credit line to the material. If material is not included in the article's Creative Commons licence and your intended use is not permitted by statutory regulation or exceeds the permitted use, you will need to obtain permission directly from the copyright holder. To view a copy of this licence, visit <http://creativecommons.org/licenses/by/4.0/>.

References

1. H. Yin, Y. Li, Z. Tian, Q. Li, C. Jiang et al., Ultra-high sensitivity anisotropic piezoelectric sensors for structural health monitoring and robotic perception. *Nano-Micro Lett.* **17**(1), 42 (2024). <https://doi.org/10.1007/s40820-024-01539-6>
2. S. Yu, T.H. Park, W. Jiang, S.W. Lee, E.H. Kim et al., Soft human-machine interface sensing displays: materials and devices. *Adv. Mater.* **35**(43), e2204964 (2023). <https://doi.org/10.1002/adma.202204964>
3. Y. Shen, X. Han, P. Zhang, X. Chen, X. Yang et al., Review on fiber-based thermoelectrics: materials, devices, and textiles. *Adv. Fiber Mater.* **5**(4), 1105–1140 (2023). <https://doi.org/10.1007/s42765-023-00267-7>
4. F. Liu, A. Christou, A.S. Dahiya, R. Dahiya, From printed devices to vertically stacked, 3D flexible hybrid systems. *Adv. Mater.* **37**(10), 2411151 (2025). <https://doi.org/10.1002/adma.202411151>
5. D. Wang, G. Ma, X. Zhang, K. Zheng, J. Zhang et al., Flexible pressure sensor composed of multi-layer textile materials for human-machine interaction applications. *ACS Sens.* **10**(1), 350–359 (2025). <https://doi.org/10.1021/acssensors.4c02583>
6. Y. Cao, P. Li, Y. Zhu, Z. Wang, N. Tang et al., Artificial intelligence-enabled novel atrial fibrillation diagnosis system using 3D pulse perception flexible pressure sensor array. *ACS Sens.* **10**(1), 272–282 (2025). <https://doi.org/10.1021/acssensors.4c02395>
7. X. Sun, J. Sun, T. Li, S. Zheng, C. Wang et al., Flexible tactile electronic skin sensor with 3D force detection based on porous CNTs/PDMS nanocomposites. *Nano-Micro Lett.* **11**(1), 57 (2019). <https://doi.org/10.1007/s40820-019-0288-7>
8. Y. Chen, Y. Zhou, Z. Hu, W. Lu, Z. Li et al., Gelatin-based metamaterial hydrogel films with high conformality for ultra-soft tissue monitoring. *Nano-Micro Lett.* **16**(1), 34 (2023). <https://doi.org/10.1007/s40820-023-01225-z>
9. Z. Xu, C. Zhang, F. Wang, J. Yu, G. Yang et al., Smart textiles for personalized sports and healthcare. *Nano-Micro Lett.* **17**(1), 232 (2025). <https://doi.org/10.1007/s40820-025-01749-6>
10. Y. Peng, J. Dong, J. Long, Y. Zhang, X. Tang et al., Thermally conductive and UV-EMI shielding electronic textiles for unrestricted and multifaceted health monitoring. *Nano-Micro Lett.* **16**(1), 199 (2024). <https://doi.org/10.1007/s40820-024-01429-x>
11. M. Du, S. Lv, J. Qiu, T. Guo, S. Zhou, Multimaterial fibers for multifunctional sensing applications. *Laser Photonics Rev.* **18**(10), 2301125 (2024). <https://doi.org/10.1002/lpor.202301125>
12. J.-H. Lee, K. Cho, J.-K. Kim, Age of flexible electronics: emerging trends in soft multifunctional sensors. *Adv. Mater.* **36**(16), e2310505 (2024). <https://doi.org/10.1002/adma.202310505>
13. Z. Liu, T. Zhu, J. Wang, Z. Zheng, Y. Li et al., Functionalized fiber-based strain sensors: pathway to next-generation wearable electronics. *Nano-Micro Lett.* **14**(1), 61 (2022). <https://doi.org/10.1007/s40820-022-00806-8>
14. P. Das, P.K. Marvi, S. Ganguly, X.S. Tang, B. Wang et al., MXene-based elastomer mimetic stretchable sensors: design, properties, and applications. *Nano-Micro Lett.* **16**(1), 135 (2024). <https://doi.org/10.1007/s40820-024-01349-w>
15. J.A. Rogers, T. Someya, Y. Huang, Materials and mechanics for stretchable electronics. *Science* **327**(5973), 1603–1607 (2010). <https://doi.org/10.1126/science.1182383>
16. J. Kim, M. Lee, H.J. Shim, R. Ghaffari, H.R. Cho et al., Stretchable silicon nanoribbon electronics for skin prosthesis. *Nat. Commun.* **5**, 5747 (2014). <https://doi.org/10.1038/ncomms6747>
17. P.-G. Su, C.-S. Wang, Novel flexible resistive-type humidity sensor. *Sens. Actuat. B Chem.* **123**(2), 1071–1076 (2007). <https://doi.org/10.1016/j.snb.2006.11.015>
18. M. Amjadi, A. Pichitpajongkit, S. Lee, S. Ryu, I. Park, Highly stretchable and sensitive strain sensor based on silver nanowire-elastomer nanocomposite. *ACS Nano* **8**(5), 5154–5163 (2014). <https://doi.org/10.1021/nn501204t>
19. W. Yan, G. Noel, G. Loke, E. Meiklejohn, T. Khudiyev et al., Single fibre enables acoustic fabrics via nanometre-scale vibrations. *Nature* **603**(7902), 616–623 (2022). <https://doi.org/10.1038/s41586-022-04476-9>
20. B. Liang, Z. Zhang, W. Chen, D. Lu, L. Yang et al., Direct patterning of carbon nanotube *via* stamp contact printing process for stretchable and sensitive sensing devices. *Nano-Micro Lett.* **11**(1), 92 (2019). <https://doi.org/10.1007/s40820-019-0323-8>

21. R. Wu, S. Seo, L. Ma, J. Bae, T. Kim, Full-fiber auxetic-interlaced yarn sensor for sign-language translation glove assisted by artificial neural network. *Nano-Micro Lett.* **14**(1), 139 (2022). <https://doi.org/10.1007/s40820-022-00887-5>
22. T. Tat, G. Chen, X. Zhao, Y. Zhou, J. Xu et al., Smart textiles for healthcare and sustainability. *ACS Nano* **16**(9), 13301–13313 (2022). <https://doi.org/10.1021/acsnano.2c06287>
23. X. Zhang, J. Chen, Z. Zheng, S. Tang, B. Cheng et al., Flexible temperature sensor with high reproducibility and wireless closed-loop system for decoupled multimodal health monitoring and personalized thermoregulation. *Adv. Mater.* **36**(45), 2407859 (2024). <https://doi.org/10.1002/adma.202407859>
24. P. Chen, H. Wu, Y. Zhao, L. Zhong, Y. Zhang et al., Quantitative assessment of fungal biomarkers in clinical samples *via* an interface-modulated optical fiber biosensor. *Adv. Mater.* **36**(21), 2312985 (2024). <https://doi.org/10.1002/adma.202312985>
25. C. Dang, Z. Wang, T. Hughes-Riley, T. Dias, S. Qian et al., Fibres-threads of intelligence-enable a new generation of wearable systems. *Chem. Soc. Rev.* **53**(17), 8790–8846 (2024). <https://doi.org/10.1039/d4cs00286e>
26. H. Lu, M. Jian, X. Liang, Y. Wang, J. Niu et al., Strong silk-worm silk fibers through CNT-feeding and forced reeling. *Adv. Mater.* **36**(49), e2408385 (2024). <https://doi.org/10.1002/adma.202408385>
27. Y. Lu, H. Zhang, Y. Zhao, H. Liu, Z. Nie et al., Robust fiber-shaped flexible temperature sensors for safety monitoring with ultrahigh sensitivity. *Adv. Mater.* **36**(18), 2310613 (2024). <https://doi.org/10.1002/adma.202310613>
28. M. Bayindir, F. Sorin, A.F. Abouraddy, J. Viens, S.D. Hart et al., Metal-insulator-semiconductor optoelectronic fibres. *Nature* **431**(7010), 826–829 (2004). <https://doi.org/10.1038/nature02937>
29. X. Cao, C. Ye, L. Cao, Y. Shan, J. Ren et al., Biomimetic spun silk ionotronic fibers for intelligent discrimination of motions and tactile stimuli. *Adv. Mater.* **35**(36), 2300447 (2023). <https://doi.org/10.1002/adma.202300447>
30. Q. Jiang, Y. Wan, Y. Qin, X. Qu, M. Zhou et al., Durable and wearable self-powered temperature sensor based on self-healing thermoelectric fiber by coaxial wet spinning strategy for fire safety of firefighting clothing. *Adv. Fiber Mater.* **6**(5), 1387–1401 (2024). <https://doi.org/10.1007/s42765-024-00416-6>
31. H. Tan, L. Sun, H. Huang, L. Zhang, R.E. Neisiany et al., Continuous melt spinning of adaptable covalently cross-linked self-healing ionogel fibers for multi-functional ionotronics. *Adv. Mater.* **36**(13), 2310020 (2024). <https://doi.org/10.1002/adma.202310020>
32. T. Sun, Y. Liang, N. Ning, H. Wu, M. Tian, Strain-insensitive stretchable conductive fiber based on helical core with double-network hydrogel. *Adv. Fiber Mater.* **7**(3), 882–893 (2025). <https://doi.org/10.1007/s42765-025-00530-z>
33. X. Wang, X. Liu, D.W. Schubert, Highly sensitive ultrathin flexible thermoplastic polyurethane/carbon black fibrous film strain sensor with adjustable scaffold networks. *Nano-Micro Lett.* **13**(1), 64 (2021). <https://doi.org/10.1007/s40820-021-00592-9>
34. D. Wang, D. Zhang, P. Li, Z. Yang, Q. Mi et al., Electrospinning of flexible poly(vinyl alcohol)/MXene nanofiber-based humidity sensor self-powered by monolayer molybdenum diselenide piezoelectric nanogenerator. *Nano-Micro Lett.* **13**(1), 57 (2021). <https://doi.org/10.1007/s40820-020-00580-5>
35. B. Yang, F.-Z. Xuan, H. Lei, Z. Wang, Y. Xiang et al., Simultaneously enhancing the IFSS and monitoring the interfacial stress state of GF/epoxy composites *via* building in the MWCNT interface sensor. *Compos. Part A Appl. Sci. Manuf.* **112**, 161–167 (2018). <https://doi.org/10.1016/j.compositesa.2018.06.006>
36. K. Wang, X. Sun, S. Cheng, Y. Cheng, K. Huang et al., Multispecies-coadsorption-induced rapid preparation of graphene glass fiber fabric and applications in flexible pressure sensor. *Nat. Commun.* **15**(1), 5040 (2024). <https://doi.org/10.1038/s41467-024-48958-y>
37. Z. Ma, Y. Wu, S. Lu, J. Li, J. Liu et al., Magnetically assisted 3D printing of ultra-antiwear flexible sensor. *Adv. Funct. Mater.* **34**(42), 2406108 (2024). <https://doi.org/10.1002/adfm.202406108>
38. Y. Wang, Y. Zhou, L. Qi, Y. Zhang, Soft optical fibers for biomedical and wearable technologies: current trends and future prospects. *Adv. Funct. Mater.* (2025). <https://doi.org/10.1002/adfm.202507712>
39. Y. Shen, Z. Wang, Z. Wang, J. Wang, X. Yang et al., Thermally drawn multifunctional fibers: toward the next generation of information technology. *InfoMat* **4**(7), e12318 (2022). <https://doi.org/10.1002/inf2.12318>
40. L. van der Elst, C. Faccini de Lima, M. Gokce Kurtoglu, V.N. Koraganji, M. Zheng et al., 3D printing in fiber-device technology. *Adv. Fiber Mater.* **3**(2), 59–75 (2021). <https://doi.org/10.1007/s42765-020-00056-6>
41. Z. Wang, T. Wu, Z. Wang, T. Zhang, M. Chen et al., Designer patterned functional fibers *via* direct imprinting in thermal drawing. *Nat. Commun.* **11**(1), 3842 (2020). <https://doi.org/10.1038/s41467-020-17674-8>
42. T. Nguyen-Dang, A.C. de Luca, W. Yan, Y. Qu, A.G. Page et al., Controlled sub-micrometer hierarchical textures engineered in polymeric fibers and microchannels *via* thermal drawing. *Adv. Funct. Mater.* **27**(10), 1605935 (2017). <https://doi.org/10.1002/adfm.201605935>
43. M. Rein, V.D. Favrod, C. Hou, T. Khudiyev, A. Stolyarov et al., Diode fibres for fabric-based optical communications. *Nature* **560**(7717), 214–218 (2018). <https://doi.org/10.1038/s41586-018-0390-x>
44. Z. Wang, L. Wei, Thermally drawn semiconductor fibers: fabrication strategies and applications. *Acc. Mater. Res.* **5**(11), 1366–1376 (2024). <https://doi.org/10.1021/accuonmsr.4c00132>
45. X. Chen, Y. Meng, S. Laperrousaz, H. Banerjee, J. Song et al., Thermally drawn multi-material fibers: from fundamental research to industrial applications. *Natl. Sci. Rev.*



- 11(10), nwae290 (2024). <https://doi.org/10.1093/nsr/nwae290>
46. S. Qian, X. Wang, W. Yan, Piezoelectric fibers for flexible and wearable electronics. *Front. Optoelectron.* **16**(1), 3 (2023). <https://doi.org/10.1007/s12200-023-00058-3>
47. S. Qian, M. Liu, Y. Dou, Y. Fink, W. Yan, A “Moore’s law” for fibers enables intelligent fabrics. *Natl. Sci. Rev.* **10**(1), nwac202 (2022). <https://doi.org/10.1093/nsr/nwac202>
48. T. Zhang, Z. Wang, B. Srinivasan, Z. Wang, J. Zhang et al., Ultraflexible glassy semiconductor fibers for thermal sensing and positioning. *ACS Appl. Mater. Interfaces* **11**(2), 2441–2447 (2019). <https://doi.org/10.1021/acsami.8b20307>
49. L. Yu, S. Parker, H. Xuan, Y. Zhang, S. Jiang et al., Flexible multi-material fibers for distributed pressure and temperature sensing. *Adv. Funct. Mater.* **30**(9), 1908915 (2020). <https://doi.org/10.1002/adfm.201908915>
50. A. Gumennik, A.M. Stolyarov, B.R. Schell, C. Hou, G. Lestoquoy et al., All-in-fiber chemical sensing. *Adv. Mater.* **24**(45), 6005–6009 (2012). <https://doi.org/10.1002/adma.201203053>
51. W. Yan, I. Richard, G. Kurtuldu, N.D. James, G. Schiavone et al., Structured nanoscale metallic glass fibres with extreme aspect ratios. *Nat. Nanotechnol.* **15**(10), 875–882 (2020). <https://doi.org/10.1038/s41565-020-0747-9>
52. C. Dong, A.G. Page, W. Yan, T. Nguyen-Dang, F. Sorin, Microstructured multimaterial fibers for microfluidic sensing. *Adv. Mater. Technol.* **4**(10), 1900417 (2019). <https://doi.org/10.1002/admt.201900417>
53. M.M. Tousi, Y. Zhang, S. Wan, L. Yu, C. Hou et al., Scalable fabrication of highly flexible porous polymer-based capacitive humidity sensor using convergence fiber drawing. *Polymers* **11**(12), 1985 (2019). <https://doi.org/10.3390/polym11121985>
54. S.D. Hart, G.R. Maskaly, B. Temelkuran, P.H. Pridaux, J.D. Joannopoulos et al., External reflection from omnidirectional dielectric mirror fibers. *Science* **296**(5567), 510–513 (2002). <https://doi.org/10.1126/science.1070050>
55. B. Temelkuran, S.D. Hart, G. Benoit, J.D. Joannopoulos, Y. Fink, Wavelength-scalable hollow optical fibres with large photonic bandgaps for CO₂ laser transmission. *Nature* **420**(6916), 650–653 (2002). <https://doi.org/10.1038/nature01275>
56. W. Yan, A. Page, T. Nguyen-Dang, Y. Qu, F. Sordo et al., Advanced multimaterial electronic and optoelectronic fibers and textiles. *Adv. Mater.* **31**(1), 1802348 (2019). <https://doi.org/10.1002/adma.201802348>
57. A. Gierej, A. Filipkowski, D. Pysz, R. Buczyński, M. Vagenende et al., On the characterization of novel step-index biocompatible and biodegradable poly(D, L-lactic acid) based optical fiber. *J. Light. Technol.* **38**(7), 1905–1914 (2020). <https://doi.org/10.1109/JLT.2019.2959945>
58. T. Iwama, Y. Guo, S. Handa, K.Y. Inoue, T. Yoshinobu et al., Thermally-drawn multi-electrode fibers for bipolar electrochemistry and magnified electrochemical imaging. *Adv. Mater. Technol.* **7**(5), 2101066 (2022). <https://doi.org/10.1002/admt.202101066>
59. C. Strutynski, R.A. Meza, L. Teulé-Gay, G. El-Dib, A. Poulon-Quintin et al., Stack-and-draw applied to the engineering of multi-material fibers with non-cylindrical profiles. *Adv. Funct. Mater.* **31**(22), 2011063 (2021). <https://doi.org/10.1002/adfm.202011063>
60. J.J. Kaufman, G. Tao, S. Shabahang, D.S. Deng, Y. Fink et al., Thermal drawing of high-density macroscopic arrays of well-ordered sub-5-nm-diameter nanowires. *Nano Lett.* **11**(11), 4768–4773 (2011). <https://doi.org/10.1021/nl202583g>
61. S. Gorgutsa, J.F. Gu, M. Skorobogatiy, A woven 2D touchpad sensor and a 1D slide sensor using soft capacitor fibers. *Smart Mater. Struct.* **21**(1), 015010 (2012). <https://doi.org/10.1088/0964-1726/21/1/015010>
62. M. Ghebrehbrhan, G.Z.J. Loke, Y. Fink, Fabrication and measurement of 3D printed retroreflective fibers. *Opt. Mater. Express* **9**(8), 3432 (2019). <https://doi.org/10.1364/ome.9.003432>
63. S. Shabahang, F.A. Tan, J.D. Perlstein, G. Tao, O. Alvarez et al., Robust multimaterial chalcogenide fibers produced by a hybrid fiber-fabrication process. *Opt. Mater. Express* **7**(7), 2336 (2017). <https://doi.org/10.1364/ome.7.002336>
64. A. Gierej, M. Vagenende, A. Filipkowski, B. Siwicki, R. Buczynski et al., Poly(D, L-lactic acid) (PDLLA) biodegradable and biocompatible polymer optical fiber. *J. Light. Technol.* **37**(9), 1916–1923 (2019). <https://doi.org/10.1109/JLT.2019.2895220>
65. M. Chen, Z. Wang, K. Li, X. Wang, L. Wei, Elastic and stretchable functional fibers: a review of materials, fabrication methods, and applications. *Adv. Fiber Mater.* **3**(1), 1–13 (2021). <https://doi.org/10.1007/s42765-020-00057-5>
66. G. Loke, W. Yan, T. Khudiyev, G. Noel, Y. Fink, Recent progress and perspectives of thermally drawn multimaterial fiber electronics. *Adv. Mater.* **32**(1), e1904911 (2020). <https://doi.org/10.1002/adma.201904911>
67. J. Zhang, Z. Wang, L. Wei, Advanced multimaterial optoelectronic fibers: a review. *J. Light. Technol.* **39**(12), 3836–3845 (2021). <https://doi.org/10.1109/JLT.2020.3036739>
68. S. Bastida, J.I. Eguiazábal, J. Nazábal, The Vicat softening temperature as a method to assess the phase behaviour of amorphous polymer blends. *Polym. Test.* **12**(3), 233–242 (1993). [https://doi.org/10.1016/0142-9418\(93\)90005-A](https://doi.org/10.1016/0142-9418(93)90005-A)
69. G. Tao, A.M. Stolyarov, A.F. Abouraddy, Multimaterial fibers. *Int. J. Appl. Glass Sci.* **3**(4), 349–368 (2012). <https://doi.org/10.1111/ijag.12007>
70. D.S. Deng, N.D. Orf, A.F. Abouraddy, A.M. Stolyarov, J.D. Joannopoulos et al., In-fiber semiconductor filament arrays. *Nano Lett.* **8**(12), 4265–4269 (2008). <https://doi.org/10.1021/nl801979w>
71. A. Canales, X. Jia, U.P. Froriep, R.A. Koppes, C.M. Tringides et al., Multifunctional fibers for simultaneous optical, electrical and chemical interrogation of neural circuits in vivo. *Nat. Biotechnol.* **33**(3), 277–284 (2015). <https://doi.org/10.1038/nbt.3093>

72. Y. Qu, T. Nguyen-Dang, A.G. Page, W. Yan, T. Das Gupta et al., Superelastic multimaterial electronic and photonic fibers and devices via thermal drawing. *Adv. Mater.* **30**(27), 1707251 (2018). <https://doi.org/10.1002/adma.201707251>
73. A. Leber, S. Laperrousaz, Y. Qu, C. Dong, I. Richard et al., Thermally drawn elastomer nanocomposites for soft mechanical sensors. *Adv. Sci.* **10**(13), e2207573 (2023). <https://doi.org/10.1002/advs.202207573>
74. J.J. Kaufman, G. Tao, S. Shabahang, E.-H. Banaei, D.S. Deng et al., Structured spheres generated by an in-fibre fluid instability. *Nature* **487**(7408), 463–467 (2012). <https://doi.org/10.1038/nature11215>
75. M. Rein, E. Levy, A. Gumennik, A.F. Abouraddy, J. Joannopoulos et al., Self-assembled fibre optoelectronics with discrete translational symmetry. *Nat. Commun.* **7**, 12807 (2016). <https://doi.org/10.1038/ncomms12807>
76. A. Sahasrabudhe, L.E. Rupprecht, S. Orguc, T. Khudiyev, T. Tanaka et al., Multifunctional microelectronic fibers enable wireless modulation of gut and brain neural circuits. *Nat. Biotechnol.* **42**(6), 892–904 (2024). <https://doi.org/10.1038/s41587-023-01833-5>
77. G. Loke, T. Khudiyev, B. Wang, S. Fu, S. Payra et al., Digital electronics in fibres enable fabric-based machine-learning inference. *Nat. Commun.* **12**(1), 3317 (2021). <https://doi.org/10.1038/s41467-021-23628-5>
78. W.M. Ryu, Y. Lee, Y. Son, G. Park, S. Park, Thermally drawn multi-material fibers based on polymer nanocomposite for continuous temperature sensing. *Adv. Fiber Mater.* **5**(5), 1712–1724 (2023). <https://doi.org/10.1007/s42765-023-00306-3>
79. Y. Zhang, Y. He, L. Niu, X. Xing, Y. Jiang et al., Enhanced sensing performance of superelastic thermally drawn liquid metal fibers through helical architecture while eliminating directional signal errors. *J. Mater. Sci. Technol.* **195**, 136–145 (2024). <https://doi.org/10.1016/j.jmst.2024.02.028>
80. A. Leber, A.G. Page, D. Yan, Y. Qu, S. Shadman et al., Compressible and electrically conducting fibers for large-area sensing of pressures. *Adv. Funct. Mater.* **30**(1), 1904274 (2020). <https://doi.org/10.1002/adfm.201904274>
81. X. Lu, H. Qu, M. Skorobogatiy, Piezoelectric micro- and nanostructured fibers fabricated from thermoplastic nanocomposites using a fiber drawing technique: comparative study and potential applications. *ACS Nano* **11**(2), 2103–2114 (2017). <https://doi.org/10.1021/acsnano.6b08290>
82. M. Qi, Y. Liu, Z. Wang, S. Yuan, K. Li et al., Self-healable multifunctional fibers via thermal drawing. *Adv. Sci.* **11**(24), e2400785 (2024). <https://doi.org/10.1002/advs.202400785>
83. I. Richard, B. Schyrr, S. Aiassa, S. Carrara, F. Sorin, All-in-fiber electrochemical sensing. *ACS Appl. Mater. Interfaces* **13**(36), 43356–43363 (2021). <https://doi.org/10.1021/acsmi.1c11593>
84. W. Jeon, J.M. Lee, Y. Kim, Y. Lee, J. Won et al., Structurally aligned multifunctional neural probe (SAMP) using forest-drawn CNT sheet onto thermally drawn polymer fiber for long-term in vivo operation. *Adv. Mater.* **36**(27), 2313625 (2024). <https://doi.org/10.1002/adma.202313625>
85. Y. Guo, S. Jiang, B.J.B. Grena, I.F. Kimbrough, E.G. Thompson et al., Polymer composite with carbon nanofibers aligned during thermal drawing as a microelectrode for chronic neural interfaces. *ACS Nano* **11**(7), 6574–6585 (2017). <https://doi.org/10.1021/acsnano.6b07550>
86. M. Kanik, M. Marcali, M. Yunusa, C. Elbuken, M. Bayindir, Continuous triboelectric power harvesting and biochemical sensing inside poly(vinylidene fluoride) hollow fibers using microfluidic droplet generation. *Adv. Mater. Technol.* **1**(9), 1600190 (2016). <https://doi.org/10.1002/admt.201600190>
87. Z. Wang, Z. Wang, D. Li, C. Yang, Q. Zhang et al., High-quality semiconductor fibres via mechanical design. *Nature* **626**(7997), 72–78 (2024). <https://doi.org/10.1038/s41586-023-06946-0>
88. J.H. Oh, S.Y. Hong, H. Park, S.W. Jin, Y.R. Jeong et al., Fabrication of high-sensitivity skin-attachable temperature sensors with bioinspired microstructured adhesive. *ACS Appl. Mater. Interfaces* **10**(8), 7263–7270 (2018). <https://doi.org/10.1021/acsmi.7b17727>
89. F. Jiao, F. Cao, Y. Gao, F. Shuang, D. Dong, A biosensor based on a thermal camera using infrared radiance as the signal probe. *Talanta* **246**, 123453 (2022). <https://doi.org/10.1016/j.talanta.2022.123453>
90. W. Yan, C. Dong, Y. Xiang, S. Jiang, A. Leber et al., Thermally drawn advanced functional fibers: new frontier of flexible electronics. *Mater. Today* **35**, 168–194 (2020). <https://doi.org/10.1016/j.mattod.2019.11.006>
91. B. Dong, Q. Shi, Y. Yang, F. Wen, Z. Zhang et al., Technology evolution from self-powered sensors to AIoT enabled smart homes. *Nano Energy* **79**, 105414 (2021). <https://doi.org/10.1016/j.nanoen.2020.105414>
92. Y. Zhou, C. Yu, X. Zhang, Y. Zheng, B. Wang et al., Ultra-sensitive ionic conductors with tunable resistance switching temperature enabled by phase transformation of polymer cocrystals. *Adv. Mater.* **36**(15), 2309568 (2024). <https://doi.org/10.1002/adma.202309568>
93. M. Bayindir, A.F. Abouraddy, J. Arnold, J.D. Joannopoulos, Y. Fink, Thermal-sensing fiber devices by multimaterial codrawing. *Adv. Mater.* **18**(7), 845–849 (2006). <https://doi.org/10.1002/adma.200502106>
94. T.Q. Trung, N.T. Tien, D. Kim, J.H. Jung, O.J. Yoon et al., High thermal responsiveness of a reduced graphene oxide field-effect transistor. *Adv. Mater.* **24**(38), 5254–5260 (2012). <https://doi.org/10.1002/adma.201201724>
95. T.Q. Trung, S. Ramasundaram, S.W. Hong, N.-E. Lee, Flexible and transparent nanocomposite of reduced graphene oxide and P(VDF-TrFE) copolymer for high thermal responsivity in a field-effect transistor. *Adv. Funct. Mater.* **24**(22), 3438–3445 (2014). <https://doi.org/10.1002/adfm.201304224>
96. L.E. Bell, Cooling, heating, generating power, and recovering waste heat with thermoelectric systems. *Science* **321**(5895), 1457–1461 (2008). <https://doi.org/10.1126/science.1158899>
97. M. Hamid Elsheikh, D.A. Shnawah, M.F.M. Sabri, S.B.M. Said, M. Haji Hassan et al., A review on thermoelectric renewable energy: principle parameters that affect their

- performance. *Renew. Sustain. Energy Rev.* **30**, 337–355 (2014). <https://doi.org/10.1016/j.rser.2013.10.027>
98. K. Meng, X. Xiao, W. Wei, G. Chen, A. Nashalian et al., Wearable pressure sensors for pulse wave monitoring. *Adv. Mater.* **34**(21), 2109357 (2022). <https://doi.org/10.1002/adma.202109357>
99. M. Kang, J. Kim, B. Jang, Y. Chae, J.-H. Kim et al., Graphene-based three-dimensional capacitive touch sensor for wearable electronics. *ACS Nano* **11**(8), 7950–7957 (2017). <https://doi.org/10.1021/acsnano.7b02474>
100. C. Wang, L. Dong, D. Peng, C. Pan, Tactile sensors for advanced intelligent systems. *Adv. Intell. Syst.* **1**(8), 1900090 (2019). <https://doi.org/10.1002/aisy.201900090>
101. T.-W. Pan, C.-W. Hsue, J.-F. Huang, Time-domain reflectometry using arbitrary incident waveforms. *IEEE Trans. Microw. Theory Tech.* **50**(11), 2558–2563 (2002). <https://doi.org/10.1109/TMTT.2002.804644>
102. E. Song, Y.-J. Shin, P.E. Stone, J. Wang, T.-S. Choe et al., Detection and location of multiple wiring faults via time-frequency-domain reflectometry. *IEEE Trans. Electromagn. Compat.* **51**(1), 131–138 (2009). <https://doi.org/10.1109/TEMC.2008.2007964>
103. B. King, N. Bruce, M. Wagih, Large-area conductor-loaded PDMS flexible composites for wireless and chipless electromagnetic multiplexed temperature sensors. *Adv. Sci.* **12**(17), 2412066 (2025). <https://doi.org/10.1002/advs.202412066>
104. J. Gamelin, A. Aguirre, A. Maurudis, F. Huang, D. Castillo et al., Curved array photoacoustic tomographic system for small animal imaging. *J. Biomed. Opt.* **13**(2), 024007 (2008). <https://doi.org/10.1117/1.2907157>
105. Q. Xu, L. Zhang, W. Liang, Acoustic detection technology for gas pipeline leakage. *Process. Saf. Environ. Prot.* **91**(4), 253–261 (2013). <https://doi.org/10.1016/j.psep.2012.05.012>
106. G.T. Clement, J. White, K. Hynynen, Investigation of a large-area phased array for focused ultrasound surgery through the skull. *Phys. Med. Biol.* **45**(4), 1071–1083 (2000). <https://doi.org/10.1088/0031-9155/45/4/319>
107. E. Song, Z. Xie, W. Bai, H. Luan, B. Ji et al., Miniaturized electromechanical devices for the characterization of the biomechanics of deep tissue. *Nat. Biomed. Eng.* **5**(7), 759–771 (2021). <https://doi.org/10.1038/s41551-021-00723-y>
108. S. Wang, T. Zhang, K. Li, S. Ma, M. Chen et al., Flexible piezoelectric fibers for acoustic sensing and positioning. *Adv. Electron. Mater.* **3**(3), 1600449 (2017). <https://doi.org/10.1002/aelm.201600449>
109. Y. Wu, Y. Ma, H. Zheng, S. Ramakrishna, Piezoelectric materials for flexible and wearable electronics: a review. *Mater. Des.* **211**, 110164 (2021). <https://doi.org/10.1016/j.matdes.2021.110164>
110. J.-H. Lee, H.-J. Yoon, T.Y. Kim, M.K. Gupta, J.H. Lee et al., Micropatterned P(VDF-TrFE) film-based piezoelectric nanogenerators for highly sensitive self-powered pressure sensors. *Adv. Funct. Mater.* **25**(21), 3203–3209 (2015). <https://doi.org/10.1002/adfm.201500856>
111. G. Tian, W. Deng, Y. Gao, D. Xiong, C. Yan et al., Rich lamellar crystal baklava-structured PZT/PVDF piezoelectric sensor toward individual table tennis training. *Nano Energy* **59**, 574–581 (2019). <https://doi.org/10.1016/j.nanoen.2019.03.013>
112. D. Yu, Z. Zheng, J. Liu, H. Xiao, G. Huangfu et al., Superflexible and lead-free piezoelectric nanogenerator as a highly sensitive self-powered sensor for human motion monitoring. *Nano-Micro Lett.* **13**(1), 117 (2021). <https://doi.org/10.1007/s40820-021-00649-9>
113. S. Egusa, Z. Wang, N. Chocat, Z.M. Ruff, A.M. Stolyarov et al., Multimaterial piezoelectric fibres. *Nat. Mater.* **9**(8), 643–648 (2010). <https://doi.org/10.1038/nmat2792>
114. N. Chocat, G. Lestoquoy, Z. Wang, D.M. Rodgers, J.D. Joannopoulos et al., Piezoelectric fibers for conformal acoustics. *Adv. Mater.* **24**(39), 5327–5332 (2012). <https://doi.org/10.1002/adma.201201355>
115. Z. Liu, S. Zhang, Z. Wu, X.-E. Wang, K. Zou et al., Visual-audio thermoelectric detectors for images and sound recognition. *Adv. Funct. Mater.* **34**(46), 2406110 (2024). <https://doi.org/10.1002/adfm.202406110>
116. T. Nguyen-Dang, A.G. Page, Y. Qu, M. Volpi, W. Yan et al., Multi-material micro-electromechanical fibers with bendable functional domains. *J. Phys. D-Appl. Phys.* **50**(14), 144001 (2017). <https://doi.org/10.1088/1361-6463/aa5bf7>
117. F. Sorin, Y. Qu, T. Nguyen Dang, W. Yan, A.G. Page et al., Super-elastic multi-material optical fibers for healthcare applications. *Optical Fibers and Sensors for Medical Diagnostics and Treatment Applications XIX*. February 2–7, 2019. San Francisco, USA. SPIE, (2019). pp. 22. <https://doi.org/10.1117/12.2510697>
118. A. Leber, C. Dong, R. Chandran, T. Das Gupta, N. Bartolomei et al., Soft and stretchable liquid metal transmission lines as distributed probes of multimodal deformations. *Nat. Electron.* **3**(6), 316–326 (2020). <https://doi.org/10.1038/s41928-020-0415-y>
119. Y. Zhang, X. Li, J. Kim, Y. Tong, E.G. Thompson et al., Thermally drawn stretchable electrical and optical fiber sensors for multimodal extreme deformation sensing. *Adv. Opt. Mater.* **9**(6), 2001815 (2021). <https://doi.org/10.1002/adom.202001815>
120. R. Qin, J. Nong, K. Wang, Y. Liu, S. Zhou et al., Recent advances in flexible pressure sensors based on MXene materials. *Adv. Mater.* **36**(24), 2312761 (2024). <https://doi.org/10.1002/adma.202312761>
121. K. Xia, Y. Tian, J. Fu, Z. Zhu, J. Lu et al., Transparent and stretchable high-output triboelectric nanogenerator for high-efficiency self-charging energy storage systems. *Nano Energy* **87**, 106210 (2021). <https://doi.org/10.1016/j.nanoen.2021.106210>
122. F.-R. Fan, Z.-Q. Tian, Z.L. Wang, Flexible triboelectric generator. *Nano Energy* **1**(2), 328–334 (2012). <https://doi.org/10.1016/j.nanoen.2012.01.004>
123. S. Niu, Z.L. Wang, Theoretical systems of triboelectric nanogenerators. *Nano Energy* **14**, 161–192 (2015). <https://doi.org/10.1016/j.nanoen.2014.11.034>

124. H.L. Wang, Z.H. Guo, X. Pu, Z.L. Wang, Ultralight ionic triboelectric mechanoreceptor with high specific outputs for epidermal electronics. *Nano-Micro Lett.* **14**(1), 86 (2022). <https://doi.org/10.1007/s40820-022-00834-4>
125. H. Zou, Y. Zhang, L. Guo, P. Wang, X. He et al., Quantifying the triboelectric series. *Nat. Commun.* **10**, 1427 (2019). <https://doi.org/10.1038/s41467-019-09461-x>
126. L. Xie, X. Chen, Z. Wen, Y. Yang, J. Shi et al., Spiral steel wire based fiber-shaped stretchable and tailorable triboelectric nanogenerator for wearable power source and active gesture sensor. *Nano-Micro Lett.* **11**(1), 39 (2019). <https://doi.org/10.1007/s40820-019-0271-3>
127. C. Dong, A. Leber, T. Das Gupta, R. Chandran, M. Volpi et al., High-efficiency super-elastic liquid metal based triboelectric fibers and textiles. *Nat. Commun.* **11**(1), 3537 (2020). <https://doi.org/10.1038/s41467-020-17345-8>
128. S.-Y. Cho, Y. Lee, H.-J. Koh, H. Jung, J.-S. Kim et al., Superior chemical sensing performance of black phosphorus: comparison with MoS₂ and graphene. *Adv. Mater.* **28**(32), 7020–7028 (2016). <https://doi.org/10.1002/adma.201601167>
129. P.C. Wanniarachchi, K.G. Upul Kumarasinghe, C. Jayathilake, Recent advancements in chemosensors for the detection of food spoilage. *Food Chem.* **436**, 137733 (2024). <https://doi.org/10.1016/j.foodchem.2023.137733>
130. C. López, Materials aspects of photonic crystals. *Adv. Mater.* **15**(20), 1679–1704 (2003). <https://doi.org/10.1002/adma.200300386>
131. A.M. Stolyarov, A. Gumennik, W. McDaniel, O. Shapira, B. Schell et al., Enhanced chemiluminescent detection scheme for trace vapor sensing in pneumatically-tuned hollow core photonic bandgap fibers. *Opt. Express* **20**(11), 12407–12415 (2012). <https://doi.org/10.1364/OE.20.012407>
132. X. An, Y. Liu, Y. Sun, X. Zhang, Y. Liu et al., Portable multifunctional sensing platform for ratiometric H₂O₂ detection and photodynamic anti-bacteria using an AIE-featured electrospinning film. *Chem. Eng. J.* **487**, 150675 (2024). <https://doi.org/10.1016/j.cej.2024.150675>
133. Y. Guo, C.F. Werner, S. Handa, M. Wang, T. Ohshiro et al., Miniature multiplexed label-free pH probe in vivo. *Biosens. Bioelectron.* **174**, 112870 (2021). <https://doi.org/10.1016/j.bios.2020.112870>
134. R. Nishimoto, Y. Sato, J. Wu, T. Saizaki, M. Kubo et al., Thermally drawn CNT-based hybrid nanocomposite fiber for electrochemical sensing. *Biosensors* **12**(8), 559 (2022). <https://doi.org/10.3390/bios12080559>
135. F. Niu, F. Zhou, Z. Wang, L. Wei, J. Hu et al., Synthesizing metal oxide semiconductors on doped Si/SiO₂ flexible fiber substrates for wearable gas sensing. *Research* **6**, 0100 (2023). <https://doi.org/10.34133/research.0100>
136. M. Cianchetti, C. Laschi, A. Menciassi, P. Dario, Biomedical applications of soft robotics. *Nat. Rev. Mater.* **3**(6), 143–153 (2018). <https://doi.org/10.1038/s41578-018-0022-y>
137. G. Tian, W. Deng, T. Yang, J. Zhang, T. Xu et al., Hierarchical piezoelectric composites for noninvasive continuous cardiovascular monitoring. *Adv. Mater.* **36**(26), e2313612 (2024). <https://doi.org/10.1002/adma.202313612>
138. S. Park, G. Loke, Y. Fink, P. Anikeeva, Flexible fiber-based optoelectronics for neural interfaces. *Chem. Soc. Rev.* **48**(6), 1826–1852 (2019). <https://doi.org/10.1039/c8cs00710a>
139. J. Kim, X. Jia, Flexible multimaterial fibers in modern biomedical applications. *Natl. Sci. Rev.* **11**(10), nwae333 (2024). <https://doi.org/10.1093/nsr/nwae333>
140. C. Sung, W. Jeon, K.S. Nam, Y. Kim, H. Butt et al., Multimaterial and multifunctional neural interfaces: from surface-type and implantable electrodes to fiber-based devices. *J. Mater. Chem. B* **8**(31), 6624–6666 (2020). <https://doi.org/10.1039/D0TB00872A>
141. Y. LeChasseur, S. Dufour, G. Lavertu, C. Bories, M. Deschênes et al., A microprobe for parallel optical and electrical recordings from single neurons in vivo. *Nat. Methods* **8**(4), 319–325 (2011). <https://doi.org/10.1038/nmeth.1572>
142. J.P. Seymour, N.B. Langhals, D.J. Anderson, D.R. Kipke, Novel multi-sided, microelectrode arrays for implantable neural applications. *Biomed. Microdevices* **13**(3), 441–451 (2011). <https://doi.org/10.1007/s10544-011-9512-z>
143. T. Saxena, L. Karumbaiah, E.A. Gaupp, R. Patkar, K. Patil et al., The impact of chronic blood–brain barrier breach on intracortical electrode function. *Biomaterials* **34**(20), 4703–4713 (2013). <https://doi.org/10.1016/j.biomaterials.2013.03.007>
144. C. Dong, Y. Zheng, K. Long-Iyer, E.C. Wright, Y. Li et al., Fluorescence imaging of neural activity, neurochemical dynamics, and drug-specific receptor conformation with genetically encoded sensors. *Annu. Rev. Neurosci.* **45**, 273–294 (2022). <https://doi.org/10.1146/annurev-neuro-110520-031137>
145. V. Emiliani, E. Entcheva, R. Hedrich, P. Hegemann, K.R. Konrad et al., Optogenetics for light control of biological systems. *Nat. Rev. Methods Primers* **2**, 55 (2022). <https://doi.org/10.1038/s43586-022-00136-4>
146. J.P. Seymour, D.R. Kipke, Neural probe design for reduced tissue encapsulation in CNS. *Biomaterials* **28**(25), 3594–3607 (2007). <https://doi.org/10.1016/j.biomaterials.2007.03.024>
147. S. Park, Y. Guo, X. Jia, H.K. Choe, B. Grena et al., One-step optogenetics with multifunctional flexible polymer fibers. *Nat. Neurosci.* **20**(4), 612–619 (2017). <https://doi.org/10.1038/nn.4510>
148. C. Lu, S. Park, T.J. Richner, A. Derry, I. Brown et al., Flexible and stretchable nanowire-coated fibers for optoelectronic probing of spinal cord circuits. *Sci. Adv.* **3**(3), e1600955 (2017). <https://doi.org/10.1126/sciadv.1600955>
149. S. Iijima, Helical microtubules of graphitic carbon. *Nature* **354**(6348), 56–58 (1991). <https://doi.org/10.1038/354056a0>
150. Y. Jang, S.M. Kim, G.M. Spinks, S.J. Kim, Carbon nanotube yarn for fiber-shaped electrical sensors, actuators, and energy storage for smart systems. *Adv. Mater.* **32**(5), 1902670 (2020). <https://doi.org/10.1002/adma.201902670>
151. J. Wang, R.P. Deo, P. Poulin, M. Mangey, Carbon nanotube fiber microelectrodes. *J. Am. Chem. Soc.* **125**(48), 14706–14707 (2003). <https://doi.org/10.1021/ja037737j>

152. A. Balena, M. Bianco, M.S. Andriani, C. Montinaro, B. Spagnolo et al., Fabrication of nonplanar tapered fibers to integrate optical and electrical signals for neural interfaces in vivo. *Nat. Protoc.* (2025). <https://doi.org/10.1038/s41596-024-01105-9>
153. M. Du, L. Huang, J. Zheng, Y. Xi, Y. Dai et al., Flexible fiber probe for efficient neural stimulation and detection. *Adv. Sci.* **7**(15), 2001410 (2020). <https://doi.org/10.1002/advs.202001410>
154. M.-J. Antonini, A. Sahasrabudhe, A. Tabet, M. Schwalm, D. Rosenfeld et al., Customizing MRI-compatible multifunctional neural interfaces through fiber drawing. *Adv. Funct. Mater.* **31**(43), 2104857 (2021). <https://doi.org/10.1002/adfm.202104857>
155. M.E.E. Alahi, M.I. Rizu, F.W. Tina, Z. Huang, A. Nag et al., Recent advancements in graphene-based implantable electrodes for neural recording/stimulation. *Sensors* **23**(24), 9911 (2023). <https://doi.org/10.3390/s23249911>
156. J. Kim, Y. Zhao, S. Yang, Z. Feng, A. Wang et al., Laser machined fiber-based microprobe: application in microscale electroporation. *Adv. Fiber Mater.* **4**(4), 859–872 (2022). <https://doi.org/10.1007/s42765-022-00148-5>
157. F. Sun, H. Jiang, H. Wang, Y. Zhong, Y. Xu et al., Soft fiber electronics based on semiconducting polymer. *Chem. Rev.* **123**(8), 4693–4763 (2023). <https://doi.org/10.1021/acs.chemrev.2c00720>
158. H. Peng, H. Li, G. Tao, L. Xia, W. Xu et al., Smart textile optoelectronics for human-interfaced logic systems. *Adv. Funct. Mater.* **34**(2), 2308136 (2024). <https://doi.org/10.1002/adfm.202308136>
159. W. Yan, Y. Qu, T. Das Gupta, A. Darga, D.T. Nguyễn et al., Semiconducting nanowire-based optoelectronic fibers. *Adv. Mater.* **29**(27), 1700681 (2017). <https://doi.org/10.1002/adma.201700681>
160. G. Loke, R. Yuan, M. Rein, T. Khudiyev, Y. Jain et al., Structured multimaterial filaments for 3D printing of optoelectronics. *Nat. Commun.* **10**, 4010 (2019). <https://doi.org/10.1038/s41467-019-11986-0>
161. L. Su, Q. Xiong, Y. Zhu, Y. Zi, A liquid–solid contact electrification based all-optical liquid flow sensor for microfluidic analysis in biomedical applications. *Adv. Funct. Mater.* **32**(45), 2207096 (2022). <https://doi.org/10.1002/adfm.202207096>
162. X. Cao, Q. Li, S. Li, X. Xu, L. Wang et al., Low-cost photoelectric flow rate sensors based on a flexible planar curved beam structure for clinical treatments. *Adv. Healthc. Mater.* **13**(19), 2304573 (2024). <https://doi.org/10.1002/adhm.202304573>
163. H. Wang, S. Li, Y. Wang, H. Wang, X. Shen et al., Bioinspired fluffy fabric with in situ grown carbon nanotubes for ultrasensitive wearable airflow sensor. *Adv. Mater.* **32**(11), 1908214 (2020). <https://doi.org/10.1002/adma.201908214>
164. M. Li, G. Qin, C. Jia, D. Zhang, Z. Li et al., Fabrication and characterization of high-sensitivity, wide-range, and flexible MEMS thermal flow velocity sensors. *Microsyst. Nanoeng.* **10**, 102 (2024). <https://doi.org/10.1038/s41378-024-00740-2>
165. J. Alvarado, J. Mireles, G. Soriano, Development and characterization of a capacitance-based microscale flowmeter. *Flow Meas. Instrum.* **20**(2), 81–84 (2009). <https://doi.org/10.1016/j.flowmeasinst.2008.12.004>
166. S. He, Z. Yang, J. Wang, X. Wang, J. Zhang et al., High-accuracy liquid flow monitoring via triboelectric nanogenerator combined with bionic design and common-mode interference suppression. *Adv. Funct. Mater.* **35**(8), 2415534 (2025). <https://doi.org/10.1002/adfm.202415534>
167. B. Chen, C. Kwok, T.N. Nguyen, Z. Wang, Integrated fiber flow sensors for microfluidic interconnects. *Adv. Mater. Technol.* **3**(11), 1800175 (2018). <https://doi.org/10.1002/admt.201800175>
168. L. Pan, Y. Xie, H. Yang, M. Li, X. Bao et al., Flexible magnetic sensors. *Sensors* **23**(8), 4083 (2023). <https://doi.org/10.3390/s23084083>
169. G.S. Cañón Bermúdez, D. Makarov, Magnetosensitive E-skins for interactive devices. *Adv. Funct. Mater.* **31**(39), 2007788 (2021). <https://doi.org/10.1002/adfm.202007788>
170. J.R. Maze, P.L. Stanwix, J.S. Hodges, S. Hong, J.M. Taylor et al., Nanoscale magnetic sensing with an individual electronic spin in diamond. *Nature* **455**(7213), 644–647 (2008). <https://doi.org/10.1038/nature07279>
171. S. Maayani, C. Foy, D. Englund, Y. Fink, Distributed quantum fiber magnetometry. *Laser Photonics Rev.* **13**(7), 1900075 (2019). <https://doi.org/10.1002/lpor.201900075>
172. Q. Zhang, Z. Ren, P. Jia, J. Shi, J. Yin et al., An ultra-miniaturized fiber humidity sensor based on near-parallel ion pathways induced efficient water–electricity conversion. *Adv. Mater.* **37**(3), 2411558 (2025). <https://doi.org/10.1002/adma.202411558>
173. Y. Zu, Z. Duan, Z. Yuan, Y. Jiang, H. Tai, Electrospun nanofiber-based humidity sensors: materials, devices, and emerging applications. *J. Mater. Chem. A* **12**(40), 27157–27179 (2024). <https://doi.org/10.1039/d4ta05042h>
174. A. Liang, X. Chen, A non-contact porous composite fiber paper-based humidity sensor for wearable breathing and skin humidity monitoring. *J. Mater. Chem. A* **12**(42), 29081–29091 (2024). <https://doi.org/10.1039/D4TA05393A>
175. L.Y. Li, Y.F. Dong, W.F. Jiang, H.F. Ji, X.J. Li, High-performance capacitive humidity sensor based on silicon nanoporous pillar array. *Thin Solid Films* **517**(2), 948–951 (2008). <https://doi.org/10.1016/j.tsf.2008.07.016>
176. W.-D. Li, K. Ke, J. Jia, J.-H. Pu, X. Zhao et al., Recent advances in multiresponsive flexible sensors towards E-skin: a delicate design for versatile sensing. *Small* **18**(7), 2103734 (2022). <https://doi.org/10.1002/sml.202103734>
177. S. Zhang, X. Yin, P. Yan, Y. Liu, X. Qi et al., Aid of smart nursing to pressure injury prevention and rehabilitation of textile cushions. *Adv. Fiber Mater.* **6**(3), 841–851 (2024). <https://doi.org/10.1007/s42765-024-00390-z>
178. J. Zhao, Z. Wei, Z. Li, J. Yu, J. Tang et al., Skin-inspired high-performance active-matrix circuitry for multimodal user-interaction. *Adv. Funct. Mater.* **31**(38), 2105480 (2021). <https://doi.org/10.1002/adfm.202105480>

179. I. You, D.G. Mackanic, N. Matsuhisa, J. Kang, J. Kwon et al., Artificial multimodal receptors based on ion relaxation dynamics. *Science* **370**(6519), 961–965 (2020). <https://doi.org/10.1126/science.aba5132>
180. M. Chen, Z. Wang, Q. Zhang, Z. Wang, W. Liu et al., Self-powered multifunctional sensing based on super-elastic fibers by soluble-core thermal drawing. *Nat. Commun.* **12**(1), 1416 (2021). <https://doi.org/10.1038/s41467-021-21729-9>
181. N. Gupta, H. Cheung, S. Payra, G. Loke, J. Li et al., A single-fibre computer enables textile networks and distributed inference. *Nature* **639**(8053), 79–86 (2025). <https://doi.org/10.1038/s41586-024-08568-6>

Publisher's Note Springer Nature remains neutral with regard to jurisdictional claims in published maps and institutional affiliations.

